Surface immobilization mechanisms of cobalt ions on hydroxyapatite catalyst supports

Corentin Reynaud, Cyril Thomas, Dalil Brouri, Yannick Millot, Antoine Miche, Guylène Costentin

Surface Immobilization Mechanisms of Cobalt ions on Hydroxyapatite catalyst supports.

Corentin Reynaud,[1] Cyril Thomas,[1] Dalil Brouri,[1] Yannick Millot,[1] Antoine Miche[1] and Guylène Costentin[1*]

[1] *Sorbonne Université, CNRS, Laboratoire de Réactivité de Surface (LRS), 4 place Jussieu, 75005 Paris, France*

*Corresponding author: guylene.costentin@sorbonne-universite.fr

Abstract

Cobalt deposition in an excess of solution was used to design Co-modified hydroxyapatite materials with various Co loadings and controlled dispersion. It is rationalized how the properties of hydroxyapatite supports (more or less stoichiometric compositions, nanorod or platelet morphologies and crystalline (100) zig-zag termination or non-apatitic hydrated external layer), influence the immobilization processes of Co by operating either with slightly acidic (natural) or basic pH of the suspension media. Four cobalt immobilization mechanisms impacting the final dispersion of Co on hydroxyapatites were identified by combining structural (XRD, ^{1}H and ^{31}P solid-state NMR, UV-Vis, Raman and X-ray fluorescence spectroscopies), surface (XPS) characterizations of Co-modified hydroxyapatites after drying and thermal treatment at 500 °C, and monitoring of the pH and the composition of the supernatant solutions during the Co deposition step. On dried Co-modified crystalline stoichiometric hydroxyapatite nanorods, cobalt is highly dispersed through cationic exchange or strong electrostatic adsorption (SEA) at slightly acidic or basic pH, respectively. After thermal treatment at 500 °C, only cation exchange preserved atomic dispersion of Co(II) ions since Co_3O_4 nanoparticles were observed on samples for which Co deposition occurred *via* SEA. On defective hydroxyapatite platelets, cobalt deposited at acidic natural pH could diffuse in an external non-apatitic layer, whereas under basic pH media, this surface layer was hydrolysed, resulting in the formation of a cobalt-substituted hydroxyapatite layer in which only a limited fraction of the surface cobalt species could be probed by XPS.

Keywords: cationic exchange; electrostatic adsorption; dissolution-precipitation; surface terminations; morphology; ss NMR; XPS; DFT

1- Introduction

Cobalt-based heterogeneous catalysts have been used for decades in hydrodesulphurization [1] and hydrodeoxygenation [2] processes, and in Fischer-Tropsch synthesis [3, 4]. Interest in such Co-based materials has been more recently extended to other reactions, such as oxidative dehydrogenation of alkanes [5-11], alkene epoxidation [12], alcohol valorization reactions [13-15], and hydrogen [16] and oxygen [17] evolution reactions. For most of these reactions, the nature of the Co species (Co oxide [7, 9] or metal [3] nanoparticles and Co isolated species [10, 18]) is a key parameter for selectivity control. These studies emphasize on how crucial is the preparation of Co-based materials with controlled Co dispersion for both their catalytic reactivity and their further resistance to sintering and leaching. Catalyst stability is an important issue for industrial applications since leaching might drastically prevent the use of Co-based materials due to the recognized Co toxicity [19]. In the context of the virtuous management of resources, Co is becoming a critical transition metal due to its increasing demand for low-carbon technologies including the production and storage of renewable energy.[19]. In the perspective of optimizing the use of Co, while minimizing its loading, the selection of a support likely to develop strong interactions with such a metal offers interesting perspectives [3].

In the last decades, the hydroxyapatite (HAp : $Ca_{10}(PO_4)_6(OH)_2$) system, a calcium phosphate, known as the main mineral component of bones and teeth, has emerged as an eco-friendly material to be used as an active phase and/or support in heterogeneous catalysis [20]. As an inexpensive material, - with low water solubility from neutral to basic pH, high thermal stability, large range of specific surface areas (SSA) and morphologies, and adjustable compositions in terms of bulk Ca/P molar ratio that enables the fine tuning of its acid-base properties [21, 22], HAp also exhibits peculiar affinity for ion substitution, such as that of the calcium cations by other divalent metals [22]. Co-modified HAp catalysts have already showed promising performance for many reactions [4, 5, 11-13, 15, 23-28]. Yet, there is a lack of structure-reactivity

relationship in this field as very little attention has been paid to the influence of the physicochemical properties of the HAp support (Ca/P molar ratios, textural properties, *etc.*) on Co speciation/dispersion. Commonly used incipient wetness impregnation [14, 15, 26] or impregnation in an excess of solution [25] procedures performed in the absence of washing steps may lead to high dispersion in particular for very low cobalt loadings [14]. Upon increasing metal loading, the initially deposited isolated species may act as nuclei for the growth of oxide clusters or particles, however [4, 25, 26]. Metal deposition in an excess of solution followed by washing steps is a common alternative procedure [5]. Although often mentioned in earlier literature studies, the existence of a cation exchange mechanism has rarely been characterized unambiguously. Cationic exchange has been also claimed in the field of HAp biomaterials, for which cobalt doping is aimed at providing antibacterial properties [29-31]. Metal sorption onto HAps in an excess of solution is much better documented in the field of environmental remediation since HAp has emerged as a promising adsorbent for the mitigation of contaminants such as heavy metals, dyes, hydrocarbons and other emerging pollutants from wastewaters and groundwaters [32, 33]. Interestingly, even if not fully understood, metal adsorption by HAps has been found to be highly efficient with particular emphasis on the absence of metal leaching [28, 29, 33]. Mostly investigated for the remediation of cadmium [34-37], copper [38] chromium [39] and lead [37], various metal immobilization modes have been reported to date depending on the metal nature and the operating conditions used. Surface-mediated processes such as cation exchange [39], surface complexation [38] and “strong metal interaction” (with nickel) when operating under basic pH [40] may take place, whereas bulk metal capture may also be involved through dissolution-precipitation processes (for Pb [38, 41] or Cd capture at high temperature [36]), which should *a priori* be detrimental for heterogeneous catalysis. Metal sorption processes have been reported to follow Langmuir isotherms [29], and to be pH dependent [37, 39, 42, 43], even though most studies have been implemented at natural pH

(without pH adjustment). The pH at which metal remediation is performed raises the question of the protonation of surface hydroxyl and phosphate groups of HAp. Although such protonation phenomena are likely to be of peculiar importance in surface complexation or strong electrostatic adsorption (SEA) processes, the influence of the isoelectric point of HAp surfaces has been scarcely discussed [42]. Rapid metal uptake, occurring within a few minutes, has been ascribed to ion exchange in the case of cobalt, copper, cadmium and lead [23, 29, 34-36, 43]. In contrast, slow additional metal uptakes occurring over a period of several days have been reported to be due to dissolution-precipitation, eventually leading to the growth of bulk copper phosphate (libethenite [29]), Cd-substituted hydroxyapatite solid solutions [34, 35] and hydroxypyromorphite [38, 39, 41]. These results emphasize how both the structural properties of HAp and the sorption conditions may impact metal remediation from wastewaters.

In the present study, the preparation of Co-modified HAp materials, with controlled Co loading and dispersion, was studied in an excess of solution and followed by washing steps. In order to vary the HAp textural/morphological properties, three HAp samples were precipitated at pH 9.0 or 6.5, and by modifying on the order of introduction of the precursors as described previously [44, 45]. Under such conditions, HAps exhibit SSA between 37 and 91 $m^2 g^{-1}$ with rod or platelet morphologies that expose similar (100) planes. Yet these HAps differ in their bulk composition (Ca/P molar ratios ranging from 1.57 to 1.75), surface terminations in terms of composition (XPS), crystallinity (HRTEM), structure (DFT calculations), surface charge (zeta potential) and dissolution ability (ICP-OES). The HAp properties, as well as the influence of the pH of the suspensions (either slightly acidic or basic) were found to significantly impact Co deposition. The thorough combination of structural (XRD, solid-state NMR, UV-Vis and Raman spectroscopies) and surface (XPS) characterizations of the dried Co-modified HAps indicates that most of the conditions used led to surface-mediated deposition processes and immobilization of highly dispersed Co species. Various Co immobilization mechanisms were found to be involved

depending on the pH deposition conditions and HAp surface terminations, impacting the final Co dispersion after thermal treatment. Chemical analysis of the related supernatant compositions after Co deposition finally enabled us to decipher the cobalt immobilization mechanisms depending on the pH conditions and on the surface properties of HAps.

2- Experimental section

2.1. Synthesis of HAp supports

Three HAp supports (~8 g batches) were obtained from precipitation at 80 °C and at stationary pH under mechanical stirring (400 rpm). In order to tune the physicochemical properties of the HAp supports, two key synthesis parameters [44-46] were varied: (i) the order of introduction of the precursors, namely the addition of the calcium solution to the phosphate one (Ca→P) or *vice versa* (P→Ca), and (ii) the stationary pH, either 9.0 or 6.5 (**Table 1**). The control of the synthesis parameters was achieved by using an automated reactor (Optimax 1001 synthesis workstation, Mettler Toledo). 400 mL of calcium and phosphate solutions with $[Ca]_0$ and $[P]_0$ initial concentrations of 0.216 and 0.130 mol L^{-1}, respectively, were prepared by dissolving $Ca(NO_3)_2 \cdot 4H_2O$ (Sigma Aldrich, purity ≥ 99.0 %) and $(NH_4)_2HPO_4$ (Acros Organics, purity ≥ 99.0 %) in ultrapure water (resistivity of 18.2 MΩ × cm at 25 °C). Depending on the target stationary pH at 80 °C, small volumes of concentrated ammonia (Sigma Aldrich, 28 %) were added at room temperature to adjust the pH of the solutions to 10.0 or 6.5 when necessary. Once the phosphate (or calcium) solution was introduced into the 1 L reactor and heated at 80 °C (5 °C/min) under mechanical stirring (400 rpm), an appropriate volume of the calcium (or phosphate) solution (corresponding to [Ca]/[P] nominal ratio of 1.67) was poured into the reactor at a controlled speed (4.4 mL min^{-1}). During this step, the pH was kept constant to 9.0 or 6.5 with the automated addition of suitable volumes of concentrated ammonia. Once the addition step was completed, a 2-hour maturation step was performed under the same pH,

temperature and stirring conditions. The reactor temperature was then cooled down to 20 °C within a few minutes and the white precipitate was recovered by centrifugation (8500 rpm). The precipitate was washed three times with distilled water to mainly remove ammonia, and ammonium and nitrate ions and subsequently dried overnight at 120 °C. The three HAp supports will be hereafter labelled to as HAp-PM_{SSA}, PM referring to as the HAp particle morphology (R and P for rods and platelets, respectively) and SSA to as the specific surface area of the support after thermal treatment at 500 °C (2.5 °C min^{-1}) for 90 minutes under Ar flow (50 mL min^{-1}) (**Table 1**).

2.2 Cobalt deposition on HAp supports

Co deposition onto the dried HAp supports was carried out in an excess of solution with various Co concentrations, deposition times and pH of the suspensions. The pH of 100 mL of ultrapure water reached about 5.4 due to CO_2 dissolution after equilibration under ambient conditions. In some cases, basification of the media was achieved by the addition of 2-5 mL of ammonia (10^{-1} mol L^{-1}) to set the pH of the solution to about 9.0. 1.00 g of the HAp support, previously dried at 120 °C, was then added and the suspension was stirred (800 rpm) for 2 h. An appropriate amount of $Co(NO_3)_2 \cdot 6H_2O$ (Sigma Aldrich, purity ≥ 98%) was then added in order to vary the target Co loading from 0.25 to 4.00 wt% and the suspension was kept under stirring for 1 h (unless otherwise stated, **Table 2**). The colour of the samples changed from white to pink-purple after addition of Co. The wet sample was recovered by centrifugation (8500 rpm) and washed three times with acetone to eliminate excess nitrate, ammonium and cobalt ions, while limiting the dissolution of the prepared Co-modified HAp surfaces. After drying at RT for 12 h, the samples were finely ground in an agate mortar, before being thermally heated under Ar flow (50 mL min^{-1}) up to 500 °C (2.5 °C min^{-1}) for 90 min. As listed in **Table 2**, the designation of the related Co-modified samples, HAp-PM_{SSA}-Co(wt%-deposition time) allows to identify the corresponding support, the deposited Co loading (wt%) and the deposition

time if different from 1 h. When basification of the initial solution was performed, the suffix "-b" was added at the end of the sample name.

2.3. Characterization techniques

Electron microscopy. TEM and HRTEM characterizations were carried out at the *Plateforme de microscopie de l'Institut des Materiaux de Paris Centre*, using a JEOL JEM 2100 microscope operating at 200 kV, emitting with a LaB_6 tip equipped with an X-ray detector (Oxford SDD X-max 80). Micrographs were recorded on a 4 K camera (Gatan Orius). The samples were firstly suspended in ethanol and dispersed with an ultrasonic bath before being rapidly deposited onto a carbon-coated copper grid. In addition, the HAp-R_{37} sample was also embedded in an epoxy resin before being cut into ultrathin slices (50-70 nm) with an ultramicrotome equipped with a diamond knife. These slices were then collected on carbon-coated copper grids.

X-ray fluorescence spectroscopy. The Ca/P bulk ratio of the HAp supports and the Co loadings (wt%) were determined by following a quantitative XRF protocol. In order to avoid matrix and grain size effects, all samples were melted into "beads" and analysed with a X-ray fluorimeter Epsilon 3xl (Panalytical) equipped with an Ag X-ray tube operating under He atmosphere under three conditions: 12 kV–25 µA for 120 s for the analysis of Ca, 10 kV–30 µA for 120 s for the analysis of P and 20 kV - 15 µA for 120 s for that of Co. The beads were prepared by mixing 0.114 g of sample, 1.231 g of fluxing agent $LiBO_2/Li_2B_4O_7$ and 0.0019 g of non-wetting agent (LiBr) in a platinum crucible. This mixture was heated at 1050 °C for 25 min in a fusion instrument (LeNeo fluxer, Claisse). Calibration curves were obtained from beads of mechanical mixtures of $Ca(NO_3)_2{\cdot}4H_2O$, $(NH_4)_2HPO_4$ and Co_3O_4. Their relative proportions were set in order to prepare reference samples with Ca, P and Co loadings close to those of the Co-modified HAp samples. The calibration curves were found to be perfectly linear over the entire concentration ranges. To validate the protocol, it was also

checked that XRF data agreed with those of ICP-OES (after mineralization of the samples with HNO_3) on selected representative samples.

N_2 sorption. Specific surface area (SSA) measurements were carried out on a BELSORP-max instrument (BEL Japan) at 77 K after evacuation of the samples at 140 °C for 12 h under vacuum. SSA was estimated by using the BET method in the $0.05 < p / p^0 < 0.30$ domain.

Inductive Coupling Plasma Optical Emission Spectroscopy. The supernatant solutions obtained after cobalt deposition were analysed by ICP-OES. After filtering (0.22 μm porosity), the supernatant solutions were diluted by a factor of 10 with diluted HNO_3 (2 vol.%), and their concentrations in Ca^{2+}, H_xPO4^{3-x} and Co^{2+} ions were determined using a 5100ICP-OES equipment (Agilent Technologies). Calibration curves were systematically plotted.

X-Ray Photoemission spectroscopy. XPS data were collected on an Omicron Argus X-Ray photoelectron spectrometer using a monochromated Al K_α ($h\nu$ = 1486.6 eV) radiation source having a 280 W electron beam power. Charge compensation was carried out using an electron beam having an energy of 1 eV and an emission current of 5 μA. The emission of the photoelectrons was analysed at a takeoff angle of 45° under ultrahigh vacuum conditions (10^{-7} Pa). XP spectra were collected with a pass energy of 20 eV for C_{1s}, O_{1s}, N_{1s}, Ca_{2p}, P_{2p} and Co_{2p} core XPS levels. After data collection, the binding energies (BE) were calibrated with respect to the BE of C_{1s} at 284.8 eV. All the reported BE were determined within an accuracy of ± 0.2 eV. The peak areas were determined after subtraction of a Tougaard background. The atomic ratio calculation was performed after normalization using Scofield factors [47]. Spectrum processing was carried out using the Casa XPS software package.

Raman spectroscopy. Raman spectra were collected with a Kaiser Optical system equipped with a charge couple detector (CCD) and a laser with λ = 785 nm. Recording conditions were adapted depending on the crystallinity of the samples: P = 12 mW, resolution = 4 cm^{-1},

accumulation time = 30 s, 30 scans per spectrum for the HAp-R_{37} and HAp-R_{88} series and P = 30 mW, resolution = 4 cm^{-1}, accumulation time = 60 s, 30 scans per spectrum for the HAp-P_{37} series.

Solid-state nuclear magnetic resonance. All the ss NMR spectra were recorded at room temperature using a Bruker Advance spectrometer operating in a static field of 11.4 T. The δ resonance frequency of ^{1}H and ^{31}P were 500.59 and 202.47 MHz, respectively. The ^{1}H and ^{31}P chemical shifts were referenced to external standards of tetra-methylsilane (TMS, Sigma Aldrich) and 85 % H_3PO_4 aqueous solution (Sigma Aldrich), respectively. A Bruker 4 mm CP MAS probe was used to perform all the experiments at a spinning speed of 14 kHz. The MAS equipment for rotation was carefully cleaned with ethanol, then dried to avoid spurious proton signals. Direct polarisation ^{31}P MAS NMR with ^{1}H high power decoupling (83 kHz) were performed with a 90° pulse duration of 2 µs, a recycle delay of 400 s and a scan number of 8. The intensities of the ^{31}P MAS spectra were normalized on the basis of the sample weight introduced into the rotor. The ^{31}P spin echo mapping spectra were recorded with a Bruker 7 mm probe in static mode using (P1 – τ – P2) sequence with P1 and P2 duration pulses of 2 and 4 µs, respectively, a recycling delay of 0.5 s, a scan number of 4096 and a τ time of 20 µs. Spectra were obtained from addition of 11 echo experiments with irradiation frequencies ranging from 700 to -300 kHz.

DFT. DFT calculations were performed using the VASP software (version 5.4.1) [48] and PBE functional in the generalized gradient approximation [49]. Atomic positions and cell parameters were optimized by reducing the total energy of the considered system. In the minimization process, self-consistent cycles were converged to 10^{-4} eV and ionic relaxation to 5×10^{-2} eV A^{-1} with quasi Newton algorithm. The reciprocal space was sampled with an automatic generation scheme for the bulk structure and limited to the gamma point for the surface calculations requiring large unit cells including 15 Å vacuum for the creation of the surfaces. The cutoff

energy for the plane waves was fixed to 400 eV in all the calculations. However, it was increased to 520 eV in the cell parameter optimization in order to avoid Pulay stress effects. Bulk structure of hydroxyapatite is usually described with the $P6_3/m$ crystallographic space group as reported in the 4317043.cif file from the Crystallographic Open Database [50]. Since both OH groups have an occupancy of 1/2 in the P63/m crystallographic space group, a derived structure with non-fractional occupancies was generated in the $P6_3/m$ space group where OH groups are all oriented in the same direction. In line with the $Ca_{10}(PO_4)_6(OH)_2$ formula, each unit cell contains 44 atoms. Their atomic positions, and *a* and *c* cell parameters were relaxed for bulk optimization. (100) surfaces were built by considering various possible cleavage planes. Corresponding slabs containing *n* structural units (*n* = 1 to 5) were separated by a *d* distance of 15 Å in order to limit their interactions. Relationship between the energy of the slab (E_{slab}), the bulk energy (E_{bulk}) and the energy for creation of (100) surface $E_{(100)}$ (two surfaces per slab) is given by **Eq. 1**:

$$E_{slab} = n\,E_{bulk} + 2\,E_{(100)} \qquad \textbf{(Eq. 1)}$$

The perfect linear relation dependence obtained between the calculated slab energies and the number of considered unit cells (**Figure S1**) validates the model construction.

Surface energy (σ) of the (100) planes could be determined by **Eq. 2**:

$$\sigma = E_{(100)}/(ac) \quad \textbf{(Eq. 2)}$$

The structures were visualized with the VESTA Software [51].

3- Results

3.1. HAp supports

Comparison of the XRD patterns (**Figure S2**) with the ICDD reference card n° 00-009-0432 indicates that the as-synthesized supports exhibit a HAp crystalline structure. As reported elsewhere [44], the changes in relative intensities of the (112) and (300) diffractions planes (2 θ = 32.20 and 32.90 °, respectively) for the samples prepared at pH 9.0 and 6.5 are attributed to their different morphologies (rods particles with hexagonal sections (R, pH 9.0) *vs* thin elongated platelets (P, pH 6.5), **Figure S3a**).The properties of the three synthesized HAp supports (**Table 1, Figures S2 and S3a**) are consistent with earlier studies in which the selected operating parameters allowed to vary the textural properties (both in terms of morphology and specific surface areas) and Ca/P ratios [44, 45].

Table 1: Precipitation conditions and properties of the HAp-PM_{SSA} supports.

Support	pH at 80 °C	Order of introduction of the reactants	Morphology	SSA (m^2 g^{-1})		Bulk Ca/P	Surface Ca/P
				Dried at 120 °C	Annealed at 500 °C		
HAp-R_{37}	9.0	P→Ca	Rods	38	37	1.75	1.27
HAp-R_{88}	9.0	Ca→P	Rods	91	88	1.68	1.24
HAp-P_{37}	6.5	Ca→P	Platelets	37	37	1.57	1.10

The HRTEM micrograph of a HAp-R_{37} rod shows an interreticular distance of 3.4 Å that is characteristic of the (002) planes of the HAp structure (**Figure 1a**). The hexagonal section of a rod particle on a micrograph of an ultramicrotome slice shows two series of crystalline planes with interreticular distances of 8.4 Å of (100) planes disoriented from 120° (**Figure 1b**). This is indicative of the exposure of (100) terminations on the elongated lateral surfaces of rod-like particles. In the case of the HAp-P_{37} platelets (**Figure 1c**), the corresponding HRTEM micrograph shows series of planes oriented at 90° with interreticular distances of 3.4 and 4.7 Å (**Figure 1b**). They are associated to the diffraction of (002) and (110) planes of the HAp structure, respectively. This indicates that (100) planes are exposed on the platelet surface. Hence, despite obvious differences in morphology depending on the pH precipitation conditions, these HAp supports mainly expose (100) planes. As already reported elsewhere

[52], the elongated rod-like particles appear well crystallized till their surface terminations (**Figure 1a**). In contrast, an external amorphous surface layer is observed for the platelets (**Figure 1c**). Such an amorphous hydrated surface layer surrounding an apatite core has been often reported in the case of biomimetic platelet apatites prepared at lower temperature and in neutral pH conditions [53]. The latter conditions are closer to those used for the preparation of HAp-P_{37} compared to those used for the preparation of HAp-R_{37}.

As commonly reported for HAps [54-56], the surface Ca/P ratios determined by XPS were found to be much lower than the bulk ones determined by XRF, *i.e.* 1.27 and 1.24 *vs* 1.75 and 1.68 for HAp-R_{37} and HAP-R_{88}, respectively (**Table 1, SI-4 Figure S4**). **Figure S4** shows that surface calcium deficiency is even more pronounced in the case of HAp-P_{37} with a surface composition (Ca/P = 1.10) comparable with that reported for an octacalcium phosphate (OCP, $Ca_8(HPO_4)_2(PO_4)_4{\cdot}5H_2O$) reference material [45]. This OCP material was first precipitated at pH 6.5 before being hydrolysed to HAp [45]. This result suggests that the hydrolysis of OCP to HAp at pH 6.5 would proceed from the core of the nanoparticles towards their surface and would remain incomplete on their surface, leaving an OCP-like hydrated layer, maybe because of its contact with the solution at pH 6.5. The presence of an OCP-like layer on the external surface of the platelets of HAp-P_{37} is further supported by ^{31}P NMR. **Figure 2** shows that the expected signal of phosphates of HAps at 2.9 ppm [52], as observed for HAp-R_{37} (**Figure 2a**, green spectrum), is shifted to 2.6 ppm for HAp-P_{37} and that an additional wide contribution of low intensity also appears at about 0 ppm (**Figure 2b**, green spectrum). These latter contributions have been previously observed on carbonated biomimetic HAps and were ascribed to the additional contributions of “OCP-like phase”, located on the external surface of the particles [57, 58].

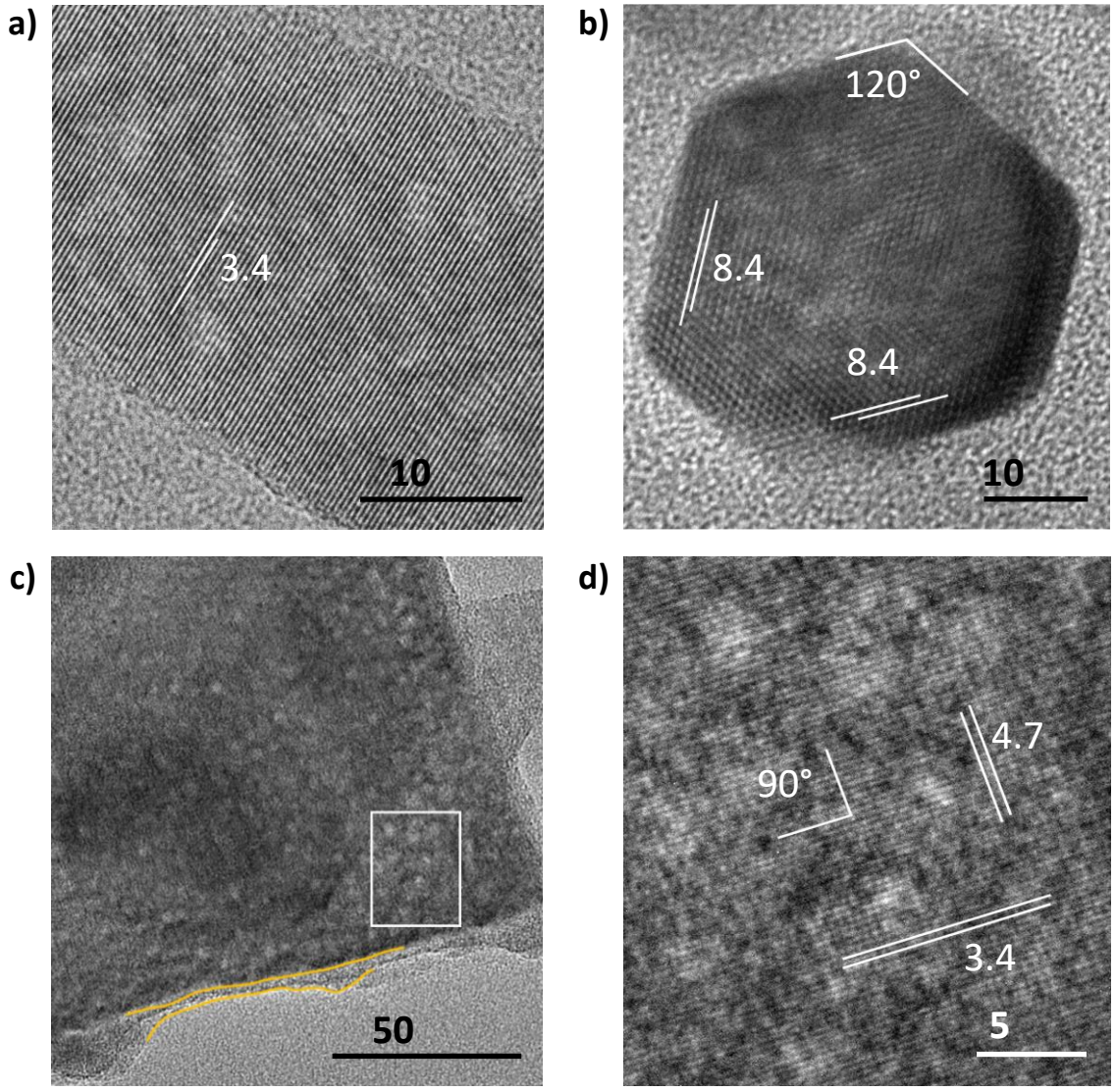

Figure 1: TEM and HRTEM micrographs of **a)** a rod of HAp-R_{37}, **b)** an ultramicrotome section of HAp-R_{37}, **c)** a platelet of HAp-P_{37} and **d)** a magnification of the white rectangle area in micrograph c.

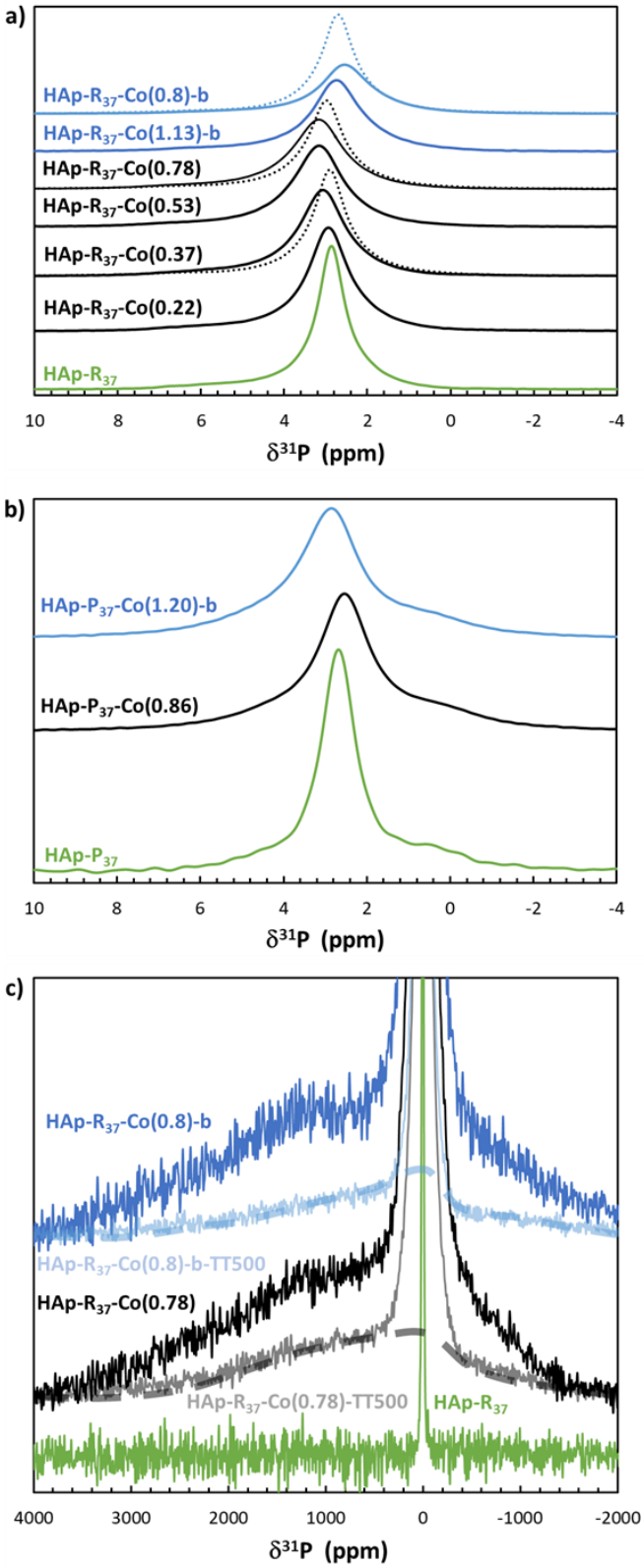

Figure 2: ^{31}P ss NMR spectra of HAp supports (green spectra), and dried (solid line) or thermally treated at 500 °C (TT500, dotted lines) Co-modified HAp samples prepared without (black spectra) and with a basic pH adjustment (blue spectra) of **a)** HAp-R_{37}-based series, **b)** HAp-P_{37}-based series and **c)** echo ^{31}P NMR experiments, for which the dashed lines show the envelop of the remaining broad signals after thermal treatment at 500 °C.

DFT calculations were carried out in order to discuss the origin of the differences between the composition of the terminated (100) crystalline surface and that in the bulk. As a first approximation, a crystal-perfect HAp is assumed for the DFT modelling and the ≡P–OH terminations (see section 3.2.3) are thus not considered. The projection of the HAp structure along the *c* crystallographic axis (**Figure 3a)** indicates that there are two types of crystallographic sites for Ca^{2+} cations, namely Ca(I) and Ca(II) depicted as dark and light blue spheres, respectively. Ca(II) cations are organized along the *c* crystallographic axis as triangles twisted from each other and delimiting an hexagonal tunnel in which the OH groups are located. As suggested by Silvester *et al.* [56], two different crystallite surface cleavage planes could be considered as indicated by the dashed lines in **Figure 3a**. Ospina *et al.* have identified two terminations by HRTEM and image simulations [59], and described them as "zig-zag" and "flat" surfaces. These two surface terminations were modelled and relaxed (**Figure 3b, 3c**). Based on linear regression (**Figure S1**) and **Eq. 1**, the energies for the creation of zig-zag and flat terminations are 4.62 and 5.31 eV, respectively. This corresponds to surface energies of 1.14 and 1.31 J m^{-2}, respectively. Hence, the zig-zag termination is found to be more stable (ΔE = -0.48 eV) than the flat one. This is an important result since only the flat termination has been considered to model HAp (100) surfaces to date [60]. Interestingly, the zig-zag termination leads to a much better agreement with the XPS experimental surface composition data listed in **Table 1** and shown in **Figure S4**. Depending on the thickness of the considered zig-zag surface, the surface Ca/P ratio varies from 1.00 to 1.67, which is compatible with the XPS data (**Table 1** and **Figure S4**). In contrast, the Ca/P ratio associated with the flat termination varies from 2.00 to 1.50 depending on the considered surface thickness in **Figure 3c.** This Ca/P ratio is therefore higher than the surface Ca/P ratio of 1.25 recorded by XPS (**Figure S4**). In addition, it must be emphasized that the zig-zag surface is the only termination that exposes OH groups.

The key role of such surface OH groups emerging from the tunnels as active basic sites in heterogeneous catalysis has been demonstrated by *in situ* and *operando* studies for HAps prepared at pH 9.0 [61-63]. All of these features strongly support the prevalence of the zig-zag termination over the flat one for the HAp crystalline surface prepared at pH 9.0 and exposing (100) crystallographic planes. Yet, such zig-zag terminations make difficult the estimation of the amount of surface accessible Ca^{2+} cations to be considered as a theoretical Ca surface density. Based on geometrical considerations only (thickness of the zig-zag termination), the Ca surface density is found to vary from 1.55 Ca nm^{-2} (considering the upper Ca(II) only with a * labelling) to 7.70 Ca nm^{-2} (including all Ca(I) and Ca(II) Ca^{2+} cations with *and ■ labellings in **Figure 3b)** [22]. Note that a surface density of about 5 Ca nm^{-2} has been reported previously based on crystallographic approaches referring to as the flat surface without considering any relaxation of the surface and without mentioning the thickness of the surface layer taken into account, however [35, 64]. Obviously, such a DFT approach could not be used to discuss the surface properties of the amorphous non apatitic surface of HAp-P_{37}.

To investigate whether this difference in exposed surfaces impacts the surface charges in aqueous medium, the zeta potential ζ of HAp-R_{37} and HAp-P_{37}, which exhibit the same SSA, was measured as a function of pH (**SI-5, Figure S5**). These measurements showed that the isoelectric points (IEP) of HAp-R_{37} (6.6) differed substantially from that of HAp-P_{37} (8.0). These differences may be attributed to specific adsorption phenomena resulting from the dissolution of the HAp supports [65-67]. The concentration of Ca^{2+} cations and phosphate species released in solution was followed by ICP-OES after 2 h of equilibration. The higher dissolution of HAp-P_{37} compared to HAp-R_{37} (**SI-5, Table S5**) can be ascribed to its higher structural defectiveness (lower bulk Ca/P ratio, **Table 1**) and to the peculiar lability of the ionic species present in the terminated non-apatitic hydrated surface layer of the platelets [22, 53]. Differences between the [Ca]/[P] concentration ratios in the supernatant solutions and the bulk

and surface Ca/P atomic ratios of HAps (**SI-5, Table S5**) indicate non-congruent dissolutions of both supports [68, 69].

Overall, the syntheses of HAps at pH 9 led to the formation of rod-like nanoparticles, whereas the synthesis performed at pH 6.5 led to the formation of platelet-like nanoparticles embedded in a poorly crystallized "OCP-like" overlayer. Such different HAp supports are used to investigate how important is the influence of the HAp morphology on the nature of the Co immobilized species under various deposition conditions.

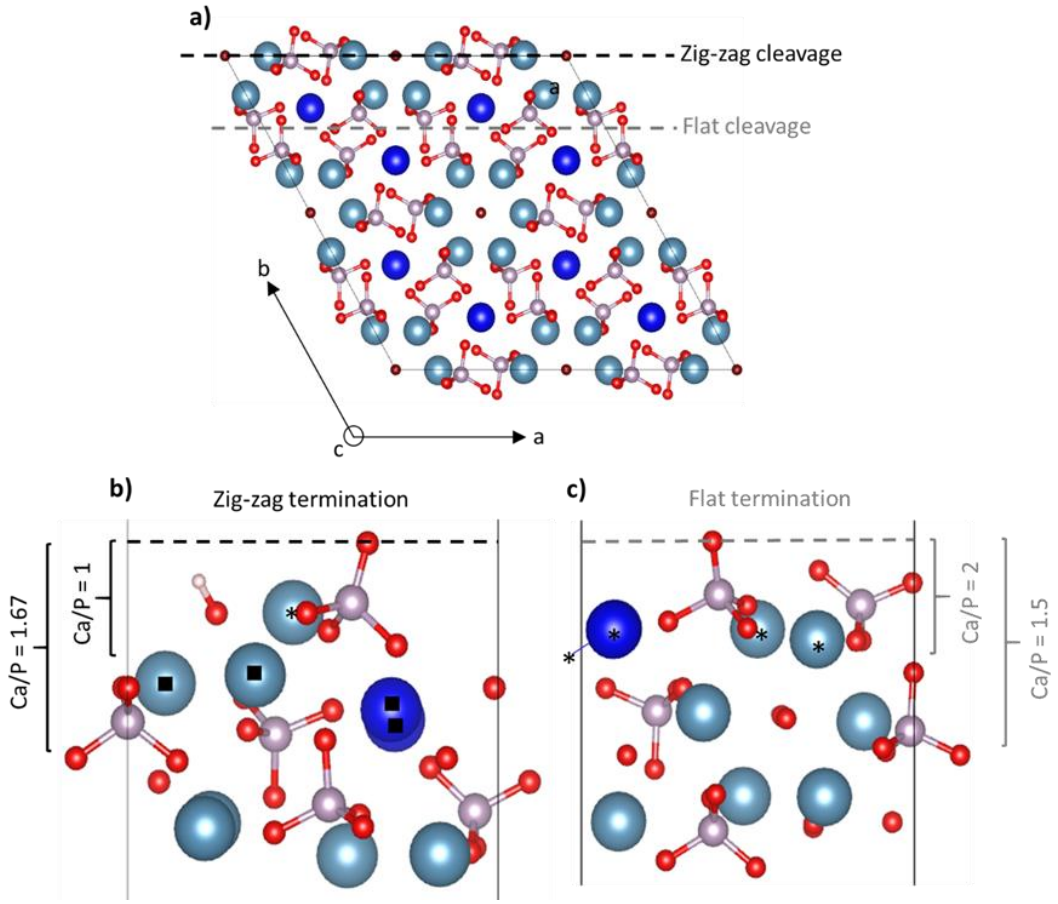

Figure 3: **a)** Projection along the [001] axis of 4 unit cells of the HAp structure in which the two cleavage planes to simulate the zig-zag and flat surface terminations for (100) faces are shown with black and grey dashed lines, respectively, **b)** the relaxed zig-zag (100) surface termination, and **c)** the relaxed flat (100) surface termination. Black and grey dashed lines show the related top surfaces. Atoms are represented as spheres, with Ca Ca(I) in dark blue, Ca(II) in light blue, O in red, P in purple and H in white. Ca^{2+} cations considered for surface Ca/P estimation are labelled with * and ■. Surface Ca density was estimated by considering either only Ca^{2+} cations labelled with * or additionally including calcium cations labelled with ■.

3.2. Cobalt deposition

Table 2 lists the various prepared Co-modified samples (see section 2.2. for sample names and related preparation conditions) and their final bulk composition ascertained by XRF.

3.2.1 Influence of the pH medium on Co loadings

3.2.1.1 Natural pH

The introduction of cobalt nitrate into the HAp-containing suspensions leads to their acidification. **Table 2** lists the minimum pH (pH_{min}) and final pH (pH_f) reached after cobalt salt addition after 1 h of equilibration, respectively. The Co deposition process operates in a moderately acidic to neutral pH range (5.7-7.1, **Table 2**) and the higher the amount of cobalt is, the lower the pH_{min} and pH_f are. Overall, for all samples, the deposited cobalt loading remains much lower than the target one (**Table 2**) and the deposition time does not significantly affect the final Co loading (HAp-R_{37}-Co(0.4-24 h) *vs* HAp-R_{37}-Co(0.37) and HAp-R_{37}-Co(0.37-10 min)). This could be attributed to the very rapid sorption process reported previously for the immobilization of metals on HAps [23, 29, 34-36]. An increase in the SSA of the HAp support leads to an increase in the deposited Co loading (**Table 2**, HAp-R_{88}-Co(1.67) *vs* HAp-R_{37}-Co(0.78)). A more reliable comparison of the various samples likely relies on the basis of their maximum Co surface densities estimated by assuming that cobalt was exclusively deposited on the surface and no pronounced dissolution-reprecipitation phenomenon occurred (**Table 2**). **Figure 4** reports on the maximum Co surface densities upon metal deposition as a function of the Co target surface densities. A similar trend is obtained for the two HAp supports exhibiting a rod-like morphology (section 3.1.). In addition, the maximum Co density of 2.15 Co nm^{-2} (**Table 2**) remains lower than that reported for cadmium immobilization without pH adjustment (~ 3 Cd nm^{-2}) [29, 36].

For the same operating deposition conditions, a slightly higher cobalt loading is deposited on HAp-P_{37} compared to HAp-R_{37} (see HAp-P_{37}-Co(0.86) *vs* HAp-R_{37}-Co(0.78) in **Table 2**). This result is consistent with the earlier work of Jaworski *et al.* reporting that Ca-deficient HAp led to a higher content of deposited cobalt [23]. Gómez-Morales *et al*. also reported that a non-

apatitic external layer may promote the lability of ions between the surface and the solution [53]. This shows that the difference in surface termination (crystallinity and composition) impacts the deposition process.

3.2.1.2 Basic pH

As claimed earlier for Ni deposition on HAp [40], basification of the HAp-containing suspensions by ammonia was performed to promote Co adsorption compared to the more acidic (natural) pH conditions. The surface of HAp-R_{37} (IEP = 6.6, **Figure S5**) should be more negatively charged at such basic pH (pH_{min} and pH_f ranging from 7.2 and 8.2 to 7.9 and 8.4, respectively, **Table 2**) than at natural pH. Note, however, that basification of the suspensions was limited to avoid the precipitation of $Co(OH)_2$, likely to occur at about pH 8.0 and 8.4 [70] upon the introduction of the Co precursor in the suspension with Co targeted loadings of 4.00 and 0.80 wt%, respectively. As illustrated in section 3.2.2.1, it could be checked by Raman spectroscopy that precipitation of $Co(OH)_2$ did not occur under the present conditions. As expected, **Table 2** shows that basification of the medium led to a significant increase in the deposited Co loading by about 45 % for HAp-R_{37}-Co(0.78) compared to HAp-R_{37}-Co(1.13)-b. In these pH conditions, the full quantity of Co could be deposited for a Co target loading of 0.80 wt% (HAp-R_{37}-Co(0.8)-b, **Table 2**), whereas at natural pH (pH ~ 6.0) full Co deposition could not be achieved for a Co target loading as low as 0.50 wt% (**Table 2**). For HAp-P_{37} (IEP = 8.0), although its surface

Table 2: Minimum (pH_{min}) and final (pH_f) pH measured after introduction of the cobalt salt in the suspensions, target and deposited Co loadings (wt%), XRF bulk Ca/P and (Ca+Co)/P ratios and cobalt surface density ($[Co]_s$) calculated by assuming *a priori* that all the Co species are located on the surface for the prepared Co-modified HAp samples. The samples underlined in grey are those prepared with basification. For each support, the samples are classified following the procedure that maximizes the deposited Co loading.

Sample name	pH_{min}	pH_f	Target Co loading (wt%)	Deposited Co loading (wt%)	Bulk Ca/P	Bulk (Ca+Co)/P	Target $[Co]_s$ (Co nm^{-2})	Maximum $[Co]_s$ (Co nm^{-2})
HAp-R_{37}-Co(1.13)-b	7.2	7.9	4.00	1.13	1.76	1.79	11.05	3.12[a]
HAp-R_{37}-Co(0.80)-b	8.2	8.4	0.80	0.80	1.80	1.82	2.21	2.21[a]
HAp-R_{37}-Co(0.78)	5.7	5.8	4.00	0.78	1.72	1.75	11.05	2.15
HAp-R_{37}-Co(0.53)	5.9	6.0	1.00	0.53	1.74	1.76	2.76	1.46
HAp-R_{37}-Co(0.4-24h)	6.2	6.3	0.50	0.40	1.76	1.78	1.38	1.10
HAp-R_{37}-Co(0.37)	6.2	6.2	0.50	0.37	1.76	1.77	1.38	1.02
HAp-R_{37}-Co(0.37-10min)	6.2	6.2	0.50	0.37	1.76	1.77	1.38	1.02
HAp-R_{37}-Co(0.22)	6.3	6.4	0.25	0.22	1.76	1.77	0.69	0.61
HAp-R_{88}-Co(1.67)	6.5	6.6	4.00	1.67	1.63	1.68	4.78	1.94
HAp-R_{88}-Co(0.88)	6.8	6.8	1.00	0.88	1.66	1.69	1.61	1.02
HAp-R_{88}-Co(0.48)	7.0	7.1	0.50	0.48	1.68	1.70	0.58	0.56
HAp-P_{37}-Co(1.20)-b	7.0	7.4	4.00	1.20	1.57	1.61	11.05	3.31[b]
HAp-P_{37}-Co(0.86)	5.6	5.7	4.00	0.86	1.56	1.58	11.05	2.38

[a] the related values should be overestimated for thermally treated samples due to Co_3O_4 formation (see section 3.2.2.1., **Figure 5**).

[b] this value should be greatly overestimated since the deposition mechanism was found to be not limited to the surface (section 3.2.2.2., **Figure 6**).

should be positively charged (minimum and final pH below 8.0, **Table 2**), the decrease in positive surface charge with increasing the pH (**Figure S5**) was also found to be beneficial for the Co deposition (HAp-P_{37}-Co(1.20)-b compared to HAp-P_{37}-Co(0.86), **Table 2**). Irrespectively of the nature of the HAp supports, such a higher ability of HAps to immobilize cobalt under basified media led to higher bulk (Ca+Co)/P ratios compared to those obtained for the corresponding Co-modified samples prepared under more acidic (natural) conditions (**Table 2**). Contrary to what is observed for natural pH conditions, the (Ca + Co)/P ratios (**Table 2**) become higher than the Ca/P of the corresponding supports (**Table 1**) under basified conditions. These different behaviours indicate that the pH applied to the HAp suspensions for Co deposition influences the immobilization mechanisms.

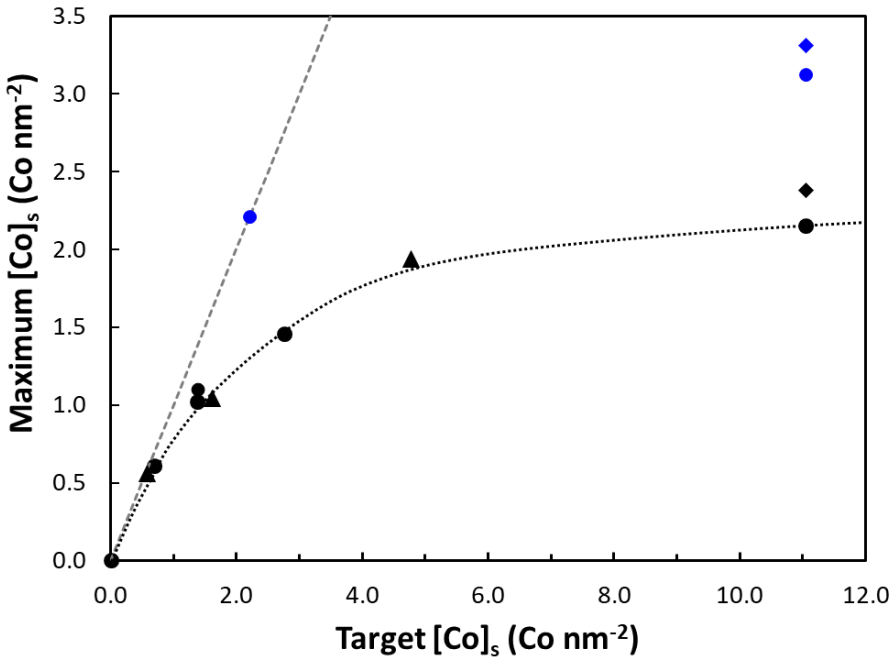

Figure 4: Evolution of the maximum Co surface density as a function of target one (calculated by assuming that all the immobilized Co species are located on the surface) on HAp-R_{37} (●), HAp-R_{88} (▲) and HAp-P_{37} (◆) where black and blue symbols stand for natural pH conditions and basified media, respectively. The dashed grey line corresponds to the linear evolution expected for a complete Co deposition on the surface.

3.2.2. Characterization of the dried and thermally treated Co-modified HAps

Co-modified HAps were characterized after drying and thermal treatment performed under Ar flow at 500 °C. This temperature was selected in the perspective of the evaluation of these catalysts at high reaction temperature, typically the highest temperature considered in the oxidative dehydrogenation of propane [71].

3.2.2.1 Structural characterizations

The textural properties of the dried and thermally treated Co-modified HAp samples were found to be similar to those of the corresponding dried and thermally treated HAp supports, respectively. This rules out any involvment of pronounced dissolution-precipitation process, as reported for Pb immobilization on HAps [38, 41]. Comparison of the XRD patterns of the supports with those of the dried and thermally treated Co-modified samples (**Figure S2**) also shows that the HAp structure is preserved after Co deposition. No crystalline cobalt oxide phase could be detected by XRD, whereas some structural modifications induced by Co deposition could be observed with other techniques.

***Colour of the Co-modified samples and UV-Vis spectroscopy*.** The colour of the dried materials changes from white to more or less intense pink purple colour with the deposition of Co. This is consistent with the earlier work of Gogoi *et al.* [43] and with representative UV-Vis spectra that show absorption bands in the 400-700 nm range (**Figure S6)**. Similar absorption range was already reported for Co(II) species [72, 73]. Thermal treatment of the samples also led to colour changes from bluish-purple for most samples to intense brownish for samples prepared in basified media (HAp-R_{37}-Co(0.8)-b and HAp-R_{37}-Co(1.13)-b). Moreover, UV-Vis spectra suggest that, beside surface dehydration leading to a better resolution of the contributions in the 450-650 nm range for all samples (**Figure S6**), a fraction of Co(II) species was oxidized to Co(III) species. This is supported by the appearance of low intense d-d transition contributions around 430 and 670 nm and a LMCT contribution in the 300-400 nm range that have been

already ascribed to Co(III) species [25, 73]. Such an oxidation process, which could be detected for the crystalline nanorods (HAp-R_{37} and HAp-R_{88} supports), is even more pronounced for HAp-R_{37}-Co(1.13)-b for which Co was deposited in a basified medium (**Figure S6a**).

Raman spectroscopy. A typical Raman spectrum of HAp is shown for the HAp-R_{37} support in **Figure 5** (green spectrum), with bands ascribed to the $\nu_{1\text{-}4}(PO_4)$ contributions [57, 74]. For all dried Co-modified HAps, the spectra were found to be similar to those of the dried HAp supports and no $Co(OH)_2$ was detected. No modification was further detected upon thermal treatment at 500 °C under Ar, except in the case of the HAp-R_{37}-Co(0.8)-b and HAp-R_{37}-Co(1.13)-b samples prepared at basic pH (**Figure 5**). Thermal treatment of the latter samples led to the appearance of a new set of intense bands at 428, 528, 625 and 694 cm^{-1} characteristic of the formation of Co_3O_4 nanoparticles [75]. This is also supported by TEM data (**SI-3, Figure S3b**, right panel) showing that Co_3O_4 particles are only formed upon thermal treatment. The presence of Co(III) ions in Co_3O_4 is thus fully consistent with the UV-Vis data (**Figure S6**) and the brownish colour of the HAp-R_{37}-Co(0.8)-b and HAp-R_{37}-Co(1.13)-b powders. Interestingly, although prepared in a basified medium, HAp-P_{37}-Co(1.20)-b does not show any cobalt oxide particles after annealing at 500 °C under Ar (**Figure S6**). This is consistent with the preservation of its purple coloration on annealing at 500 °C that is observed for all the dried samples due to d-d transitions of Co(II) species in the 450-650 nm range (**Figure S6c**).

ss NMR.

Contrary to UV-Vis and Raman spectroscopies that could reveal some structural differences only on thermally treated Co-modified HAps samples, the comparison of ss NMR spectra recorded on dried Co-modified HAps samples clearly shows differences induced by the Co deposition protocols. The changes in the direct polarisation of the ^{31}P and ^{1}H NMR signals observed in the presence of Co (peak intensity, chemical shift and full width at half maximum

in **Figure 2a, Figure 2b** and **Figure S7**)) are attributed to perturbations induced by d^7 paramagnetic Co(II) species [76-78].

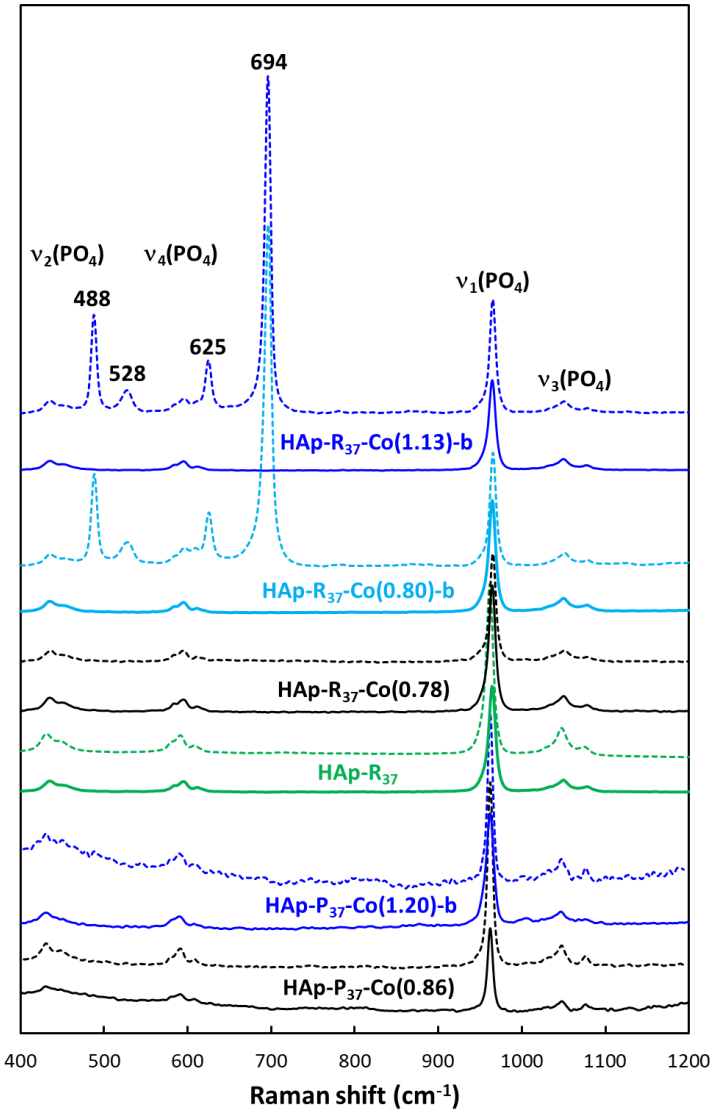

Figure 5: Raman spectra of dried HAp-R_{37} support (green spectrum) and selected Co-modified HAp-R_{37} and HAp-P_{37} samples. Solid and dashed lines are used for dried and thermally treated samples, respectively. Black and blue spectra stand for cobalt deposition achieved without and with basification of the medium, respectively.

Firstly, the decrease in the area of the NMR signals with increasing Co loading (**Figure 2a and Figure 2b** and **Figure S7**) shows that some of the P atoms are not detectable by direct polarization NMR, due to their close proximity to the Co(II) species. The corresponding "lost" fraction of the ^{31}P signal could however be observed by applying the spin mapping technique, which consists in reconstructing the spectrum of an extremely broad line from several echo

spectra (**Figure 2c**). The large width of the ^{31}P signal (~3000 ppm) indicates a strong paramagnetic interaction and hence, a proximity between these P atoms and the Co(II) deposited species.

Secondly, the P and H species far enough from the deposited Co(II) species are still monitored by direct polarization (**Figure 2a, Figure 2b** and **Figure S7**), but exhibit different shifts of the main ^{31}P and ^{1}H contributions compared to those of the supports depending on the deposition conditions. For the dried crystalline HAp-R_{37} series, the deposition of increasing amounts of Co carried out without adjustment of the pH medium (black spectra in **Figure 2a**) monotonously shifts the ^{31}P signals to higher chemical shifts compared to that of the HAp support (green spectrum in **Figure 2a**). Such a Co deposition also results in a broadening and a decrease in the intensity of the ^{31}P signals. In contrast, the ^{31}P signals shift to lower chemical shifts with the deposition of Co carried out with basification of the medium prior to introduction of the Co precursor salt (blue spectra in **Figure 2a**). Opposite ^{31}P shifts are observed when Co is immobilized on the platelet-like HAp nanoparticles (HAp-P_{37}, **Figure 2b**) compared to those observed on the rod-like HAp nanoparticles (HAp-R_{37}, **Figure 2a**). It must be noted that similar changes in shift and intensity of the ^{31}P signals are also observed for ^{1}H signals of the two Co-modified HAps (**SI-7, Figure S7**). Such a comparison of the perturbations induced by cobalt deposition on HAps on the ^{31}P (**Figure 2a** and **2b**) and ^{1}H (**Figure S7**) signals suggests that Co and P show a quite comparable proximity [79] in the HAp-R_{37}-Co(x) series and in HAp-P_{37}-Co(1.20)-b on the one hand, and in HAp-P_{37}-Co(0.86) and in the HAp-R_{37}-Co(x)-b series on the other hand.

After thermal treatment, the perturbations induced by the paramagnetic Co(II) species on the ^{31}P NMR contributions are significantly reduced (**Figure 2a, Figure 2c**). Under both pH conditions for the HAp-R_{37} support, Co deposition results in (i) an increase in the intensity of the ^{31}P signal, (ii) a modification of ^{31}P chemical shift almost back to that found for the HAp

support, (**Figure 2a**) and (iii) a decreased contribution in echo experiments (**Figure 2c)**. Such changes are consistent with a decrease in the number of Co(II) paramagnetic centers due to partial oxidation of Co(II) to Co(III) cations occurring upon the thermal treatment, as supported by Co_3O_4 formation detected by Raman spectroscopy for HAp-R_{37}-Co(0.8)-b and HAp-R_{37}-Co(1.13)-b (**Figure 5**) and by the evolution of UV-Vis spectra after thermal treatment for the other samples (**Figure S6**).

3.2.2.2 Surface characterizations

XPS spectra of dried Co-modified HAps show a contribution between 775 and 815 eV characteristic of the presence of Co(II) species. As already noted for the Ca/P ratios of the HAp supports (**Table 1**), the surface (Ca+Co)/P ratios of Co-modified HAps remain systematically lower than the bulk ones (**SI 8, Table S8**). Basification of the suspension media prior to Co deposition leads to materials with higher surface (Ca+Co)/P ratios compared to those for which Co deposition was carried out under natural pH conditions, except in the case of the HAp-P_{37} support. In this latter case, despite a higher Co loading was deposited, dried HAp-P_{37}-Co(1.20)-b shows a lower (Ca+Co)/P surface ratio compared to that measured for the dried HAp-P_{37}-Co(0.86) sample (1.40 and 1.45, respectively, **Table S8**).

Thermal treatment of the Co-modified HAp samples at 500 °C led to a decrease in the (Ca+Co)/P ratios compared to the dried samples **(Table S8)**, as also observed for the Ca/P ratios of the HAp supports (**Table 1**). This may be attributed to the relaxation of the Ca^{2+} and Co^{2+} cations towards the inner subsurface compared to phosphates. Comparison of the Co/(Ca+Co) surface ratios measured for dried and thermally treated samples (**Figure 6**) shows that Co should be even more inner-relaxed compared to calcium upon thermal treatment since these ratios are significantly lowered. The more pronounced inner relaxation of Co might be ascribed to its lower ionic radius compared to Ca (76 and 99 pm, respectively).

For dried samples, the linear relationship between the Co/(Ca+Co) ratios measured by XPS and the Co density (dotted line in **Figure 6a**) obtained for most of the samples shows that well dispersed Co-deposited species could be similarly probed by XPS except for HAp-P_{37}-Co(1.20)-b (**Figure 6b**, blue diamond). After thermal treatment at 500 °C, such a high Co dispersion is maintained for samples prepared at natural pH, as deduced from by the linear relationship (**Figure 6b)**. In contrast, thermal treatment results in a loss of cobalt dispersion for HAp-R_{37}Co(0.8)-b and HAp-R_{37}-Co(1.13)-b (**Figure 6b**, blue dot), which is consistent with the formation of Co_3O_4 nanoparticles on these samples (**Figure 5**). The formation of such Co_3O_4 nanoparticles (**SI-3, Figure S3b**, right panel) indicates that the cobalt densities of 2.21 and 3.12 Co nm^{-2} reported in **Table 2** must be overestimated for the thermally treated HAp-R_{37}-Co(0.8)-b and HAp-R_{37}-Co(1.13)-b samples.

The cobalt density reported in **Table 2** for HAp-P_{37}-Co(1.20)-b (3.31 Co nm^{-2}) must be also overestimated as the Co/(Ca+Co) ratios of this sample deviate from the linear relationships found for the other samples in **Figure 6**, both after drying and thermal treatment. Given that neither $Co(OH)_2$ nor Co_3O_4 formation could be detected on the dried and thermally treated HAp-P_{37}-Co(1.20)-b samples, the lower Co/(Ca+Co) ratios may be attributed to a screening of the Co XPS signal by Ca^{2+} and $H_xPO_4^{3-x}$ species and the corresponding burial of Co in a surface layer due to a deep restructuration of the surface after Co deposition. If all of the Co species of the thermally treated HAp-P_{37}-Co(1.20)-b sample had been probed as efficiently as in the HAp-R_{37}-Co(*x*) and HAp-R_{88}-Co(*x*) series (linear correlation in **Figure 6b**), the HAp-P_{37}-Co(1.20)-b sample should have exhibited a much higher Co/(Ca + Co) ratio (0.104) than that measured experimentally (0.056 in **Figure 6b**, blue diamond). This suggests that only about half of the Co species was probed by XPS in this particular sample.

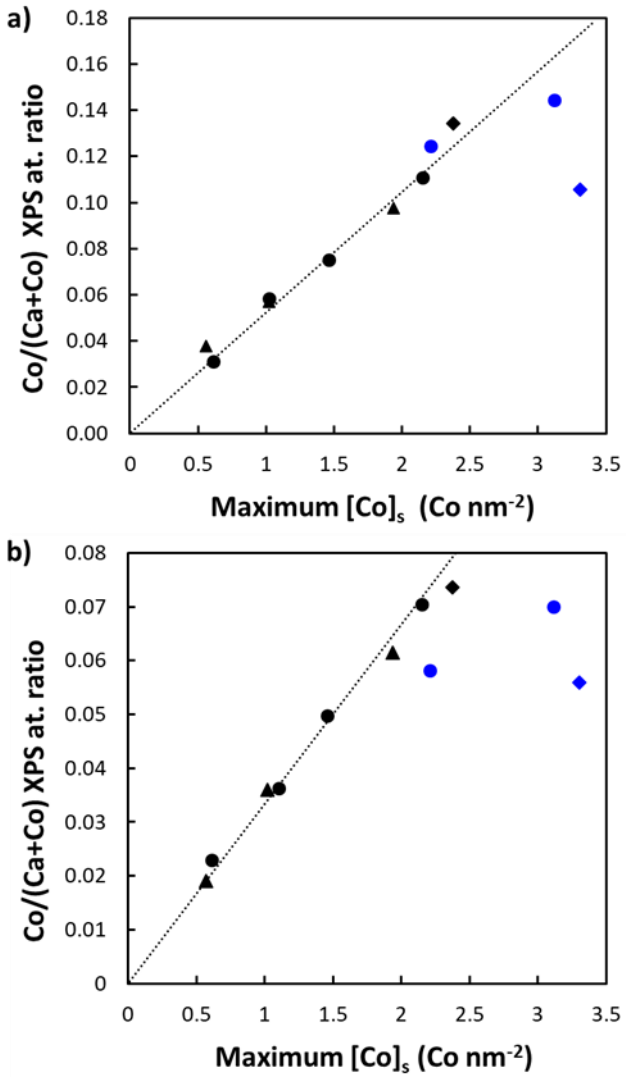

Figure 6: Surface Co/(Ca+Co) ratios measured by XPS as a function of the maximum Co surface density (**Table 2**) calculated by assuming that all the deposited Co species (Co wt%) are located exclusively on the HAp surface and efficiently probed by XPS **a)** on dried samples **b)** on samples thermally treated at 500 °C. ●, ▲ and ◆ correspond to Co-modified HAps for Co deposition onto HAp-R_{37}, HAp-R_{88}, and HAp-P_{37}, respectively; black and blue symbols stand for natural pH and basified medium, respectively.

3.2.3 Monitoring of the solutions during the Co deposition processes

The characterization of Co-modified HAps in dried and thermally treated states by various techniques indicates that the Co species should be present in various chemical environments onto the HAp supports likely due to the occurrence of various Co deposition mechanisms. As reported in **Table 2**, the pH of the media is modified during the Co deposition processes. Typical pH profiles are described in **SI-9**. The predominance diagram of surface HAp

terminations proposed by Wu *et al.* [42] shown in **Figure 7** indicates that crystalline surfaces (HAp-R_{37} and HAp-R_{88}) must be mainly terminated by ≡P–OH and ≡Ca–OH_2^+ groups below pH 6.7, which is typically the case for Co deposition at natural pH, and by ≡P–O^- and ≡Ca–OH_2^+ groups after basification of the medium. The data for the pK_a of ≡Co–OH_2^+/≡Co–OH could not be found, but must be close to 9.82 (**SI-9**, **Eq. S9-1**) [80].

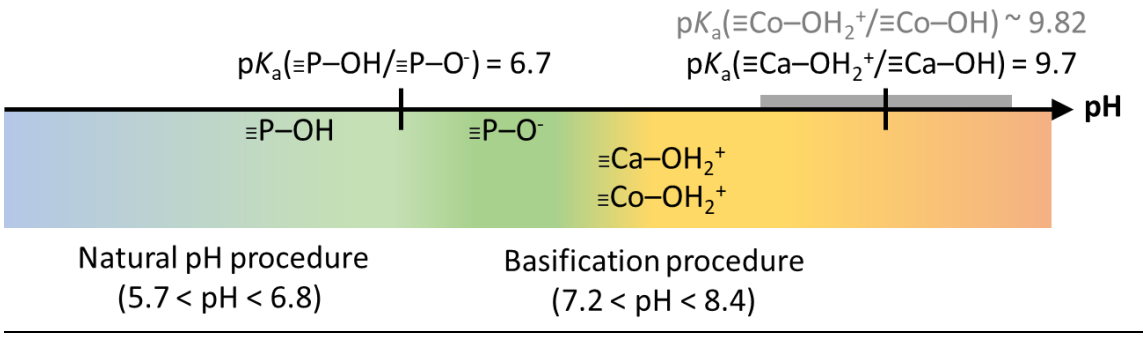

Figure 7: Predominance diagram of surface Ca and P terminations for HAp at the solid-liquid interface deduced from the surface complexation model of Wu *et al.* [42]. By assuming that the pK_a of ≡Co–OH_2^+/≡Co–OH is close to the equilibrium described in **Eq. S9-1** [80], ≡Co–OH_2^+ termination must be the more likely in the pH range explored in the present study.

The chemical composition of the supernatant solutions was complementary investigated after Co deposition to achieve material balance. The total concentrations in released ions ($[Ca]_t$ and $[P]_t$) and the final concentration in Co^{2+} ions remaining in the solutions ($[Co]_f$) were analysed by ICP-OES. The total quantity of phosphate species released in the solution ($[P]_t$) after a given Co deposition time results only from the dissolution of the HAp supports ($[P]_t = [P]_{diss}$). In contrast, the total quantity of Ca^{2+} cations released in the solutions ($[Ca]_t$, **Eq. 3**) results from the partial dissolution of HAps as $[Ca]_{diss}$ (see section 3.2.3.1. and **Table S5**) and/or release of Ca^{2+} cations in the reacting medium associated with the substitution of Ca^{2+} cations ($[Ca]_{sub}$) from the HAp support for Co^{2+} cations. Whether the substitution step proceeds through a surface-mediated process or a deeper restructuration process, such a step corresponds to cation exchange ($[Ca]_{sub} = [Ca]_{exc}$) or dissolution-precipitation, respectively, in which the material Ca balance should be written as.

$$[Ca]_t = [Ca]_{diss} + [Ca]_{sub} \qquad \textbf{(Eq. 3)}$$

3.2.3.1 HAp dissolution

Figure 8a shows the concentration in phosphate species released in the solution ($[P]_{diss} = [P]_t$) due to HAp dissolution as a function of the final pH (pH_f) of the medium after Co deposition (**Table 2**). **Figure 8a** indicates that HAp-P_{37} (◆), which exhibits the lowest bulk Ca/P ratio (**Table 2**), is found to be the most prone to dissolution both in the presence and in the absence of cobalt. As expected [44], **Figure 8a** also shows that the dissolution of HAps increases as the pH decreases. In particular, basification of the suspensions prior to the addition of the Co precursor salt obviously limits HAp dissolution. The concentration in phosphate species in the supernatant solution appears to be below the detection limit of ICP-OES (~ 1 ppm, $[P]_t \approx 5 \times 10^{-5}$ mol L^{-1}) for HAp-R_{37}-Co(1.13)-b (○ in **Figure 8a**) and for the HAp-R_{88}-Co(*x*) samples (△ in **Figure 8a**). For the latter samples, the very low concentration of P species close to the detection limit of ICP-OES is consistent with the peculiar resistance of stoichiometric HAp to dissolution.

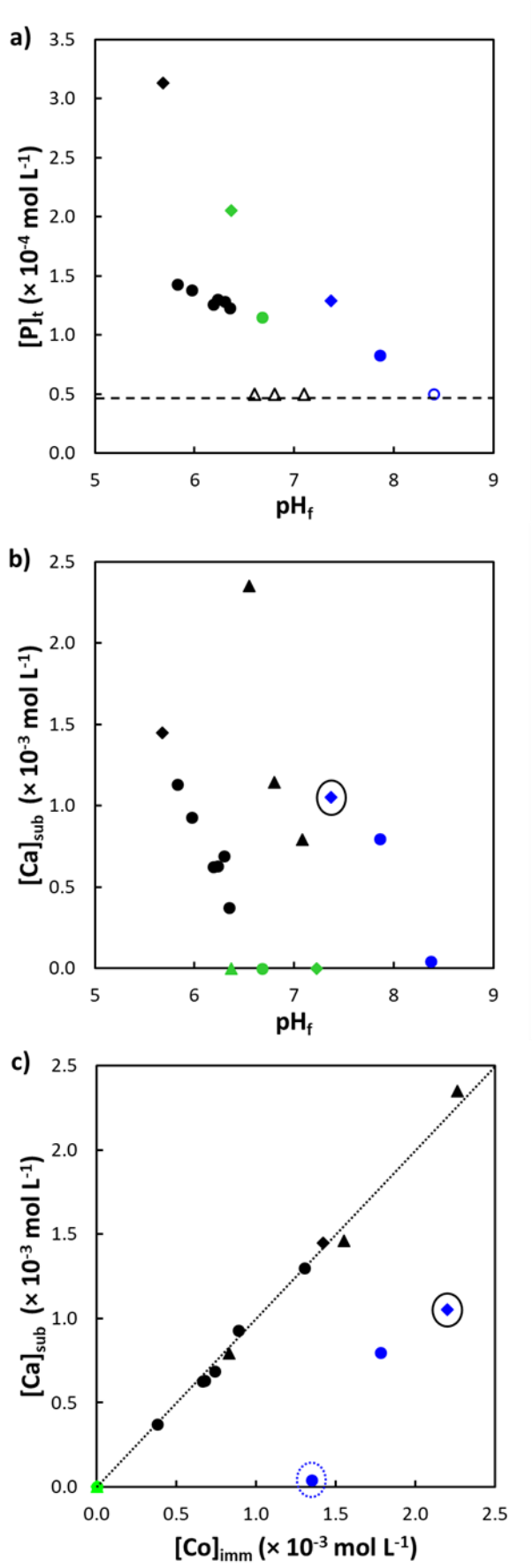

Figure 8: a) concentration in phosphate species released in the supernatant solutions as a function of the final pH of the medium after Co immobilization with the dashed

horizontal line corresponding to the detection limit of phosphate species by ICP-OES, **b)** concentration in Ca^{2+} cations released through cationic substitution estimated from (**Eq. 4**), as a function of the final pH of the medium after Co deposition, **c)** concentration in Ca^{2+} cations released through substitution process as a function of concentration of immobilized Co^{2+} cations.
●, ▲ and ◆ symbols correspond to samples for which Co immobilization was carried out onto HAp-R_{37}, HAp-R_{88}, and HAp-P_{37} supports, respectively; green symbols correspond to experiments carried out without introduction of Co precursor salt in the HAp-containing suspensions, black and blue symbols correspond to experiments performed without (natural pH) and with basification of the suspensions in which the Co precursor salt was introduced, and empty symbols are used to report an overestimated $[P]_t$ concentration considered to be close to the detection limit. $[Ca]_{sub} = [Ca]_{exc}$, except for HAp-P_{37}-Co(1.20)-b sample that is identified by a black circle and for which the reported Ca concentration rather originates from deeper substitution process (dissolution-reprecipitation). Blue dotted circle identifies the HAp-R_{37}-Co(0.80)-b sample for which almost only SEA takes place since negligible substitution was detected.

3.2.3.2 Co immobilization by substitution

Given that HAp dissolution was shown to be non-congruent (section 3.1., **Table S5**), and assuming that the D_{nc} non-congruent dissociation parameter ($D_{nc} = [Ca]_{diss}/[P]_{diss}$) remains essentially constant in the considered pH_f range for a given support (D_{nc} = 0.87 and 1.22 for HAp-R_{37} and HAp-P_{37}, respectively, **Table S5**), the $[Ca]_{sub}$ concentration in Ca^{2+} cations originating from substitution processes can be deduced via **Eq. 4**.

$$[Ca]_{sub} = [Ca]_t - [Ca]_{diss} = [Ca]_t - D_{nc}[P]_t \qquad \textbf{(Eq. 4)}$$

Figure 8b shows the evolution of the $[Ca]_{sub}$ concentration as a function of pH_f. Ca substitution was found to occur for all the Co-modified HAp samples, except in the case of HAp-R_{37}-Co(0.8)-b ($[Ca]_{sub} \sim 0$ mol L^{-1}). The data obtained in **Figure 8b** together with the analysis of the $[Co]_f$ concentration in the supernatant solutions allowed to plot the concentration in Ca^{2+} ions released in solution ($[Ca]_{sub}$) upon cationic substitution as a function of the concentration in immobilized cobalt cations ($[Co]_{imm}$ in **Eq. 5**) in **Figure 8c**.

$$[Co]_{imm} = [Co]_i - [Co]_f \qquad \textbf{(Eq. 5)}$$

where $[Co]_i$ and $[Co]_f$ are the initial and final concentrations of cobalt introduced in the deposition solution and remaining in the supernatant solution, respectively.

For all the samples prepared at natural pH (HAp-R_{37}-Co(*x*), HAp-R_{88}-Co(*x*) and HAp-P_{37}-Co(0.86) series), **Figure 8c** (black symbols) shows a remarkable correlation between the concentration in Ca released upon substitution and that of immobilized Co onto the HAp surface ($[Ca]_{sub} = [Co]_{imm}$). This correlation is further supported by the comparable (Ca+Co)/P and Ca/P ratios in the Co-modified HAp samples and the corresponding HAp supports, respectively, (**Table 2** *vs* **Table 1**). For both HAp-R_{37}-Co(*x*) and HAp-R_{88}-Co(*x*) series prepared at natural pH, for which the immobilization is a purely surface mediated processes (**Figure 6a**), the substitution corresponds to a cationic exchange process. As discussed in **SI-9**, the cationic exchange may occur directly (without any change in pH according to **Eq. S9-2**). Besides, the observed transient pH acidification (**Figure S9a**, A2 region) also suggests that a protonic exchange process between ≡P–OH and Co^{2+} species (**Eq. S9-3**) could also be a transient step toward cationic exchange between Ca^{2+} and Co^{2+}.

3.2.3.3 Co immobilization by SEA

A different behaviour is observed when basification of the HAp suspensions was carried out prior to the introduction of the cobalt precursor salt (**Figure 8**), although Co deposition occurred on the surface only for HAp-R_{37}-Co(*x*)-b (•) (**Figure 6a**). **Figure 8c** shows that the concentrations in Ca^{2+} cations released from cation substitution ($[Ca]_{sub}$) of HAp-R_{37}-Co(*x*)-b (•) are lower than those of immobilized Co^{2+} cations ($[Co]_{imm}$). The higher bulk (Ca+Co)/P ratios are observed for such samples (**Table 2**) compared to the bulk Ca/P ratios of the corresponding HAp supports (**Table 1**) therefore indicates that a SEA process must also be involved in a basic medium (**Eq. 4**). In the case of a very low Co loading (HAp-R_{37}-Co(0.80)-b, blue dotted circle in **Figure 8c**), a SEA mechanism takes place almost exclusively as

negligible Ca^{2+} cations were released in the supernatant solution ($[Ca]_{sub} \sim 0$ mol L^{-1} in **Figure 8c**), whereas for higher Co loadings, both mechanisms must be co-existing ($[Ca]_{sub} > 0$ mol L^{-1} in **Figure 8c**). The observed decrease in Ca^{2+} cations released ($[Ca]_{sub}$) in the supernatant solutions with increasing the final pH of the suspension (**Figure 8b**) indicates that the SEA process should be favoured over that of cationic exchange as the pH increases.

4- Discussion: Co immobilization mechanisms

Figure 9 summarizes the proposed mechanisms of Co immobilization depending on both the surface properties of the synthesized HAps and the pH conditions applied for Co deposition.

4.1 Rod-like HAp particles

4.1.1 Co immobilization at natural pH

Rod-like particles of HAps prepared by precipitation at 80 °C and pH 9.0 expose (100) surface with crystalline zig-zag terminations. The increase in SSA, achieved by varying the order of introduction of the HAp precursors during precipitation (**Table 1**), allows to increase the deposited Co loading (**Table 2**). At natural pH (moderately acidic to neutral pH conditions depending on the Co concentration in the solution, as no basification of the medium was carried out prior to the introduction of the Co precursor salt), samples prepared with the stoichiometric HAp-R_{88} support appear to be very stable in solution ($pH_f > 6.4$) (**Figure 8a**, △). In contrast, a very small concentration in $[P]_{diss}$ and $[Ca]_{diss}$, issued from non-congruent dissolution of the surface of the over-stoichiometric HAp-R_{37} support (**Table S5**), can be measured in the supernatant solution ($pH_f < 6.4$, **Figure 8a**, •). The remarkable agreement between the quantity of Ca^{2+} cations released in solution and the quantity of Co immobilized onto the HAp supports during the Co deposition experiments (**Figure 8c**), associated with the identification of a surface-mediated process attested by XPS (**Figure 6a**), demonstrates the involvement of a cationic exchange mechanism for Co immobilization with the substitution of surface Ca^{2+}

cations of HAp for Co^{2+} cations (**Figure 9a)**. Such a cationic exchange may proceed either directly or may be also assisted by transient protonic exchange of the surface ≡P–OH terminations by Co^{2+} cations (**Eqs. S9-3** and **S9-4**), as suggested by the acidification step in the course of Co deposition (A_2 region in **Figure S9a**). The occurrence of a surface-mediated cationic exchange process is also supported by the fairly comparable final bulk (Ca+Co)/P and Ca/P ratios in Co-modified HAps **(Table 2**) and the corresponding rod-like HAp supports (**Table 1**), respectively. Co ions must therefore be immobilized as single atoms located in substitution of the Ca^{2+} cationic surface sites (**Figure 9a**). Such a substitution process must provide high surface cohesion, explaining the thermal stability of such species. Annealing of the samples at 500 °C did not result in their sintering into Co oxides (**Figure 5**) and preserved them as atomically dispersed Co species. The surface cobalt density was found to remain below the Ca surface density estimated for a zig-zag (100) termination if one includes both Ca(I) and Ca(II) sites labelled with * and ■ in **Figure 3b**.

4.1.2 Co immobilization in a basified medium

When basification of the HAp-containing suspensions was achieved prior to the introduction of the cobalt precursor salt, the more negatively-charged surfaces (pH > IEP, **Figure S5**) immobilized a higher Co content compared to the experiments carried out at natural pH (**Figure 8c**). XPS analysis of the dried samples (**Figure 6a**) indicates that (i) a surface immobilization mechanism should take place under such basic conditions. However, (ii) the lower amount of calcium released in solution compared to the quantity of Co immobilized onto the HAp supports during the Co deposition experiments (**Figure 8c**), and (iii) the increase of the (Ca+Co)/P ratios in the Co-modified HAps compared to the Ca/P ratios of the corresponding HAps (**Table 2** *vs* **Table 1**), indicates that Co is deposited via a SEA mechanism at least in part (**Figure 9b**). Note that in such conditions, this adsorption process on ≡P–O^- terminations (**Figure 7**) does not impact the pH (**Eq. S9-5**), explaining that only two regions are observed in the corresponding

pH profile (**Figure S9-b**). At the lowest Co loading (HAp-R_{37}-Co(0.8)-b), SEA is almost exclusively observed as negligible Ca^{2+} was released in the supernatant solution (**Figure 8b**). In contrast, as the Co loading increases, an additional fraction of Co is also immobilized by cationic exchange (**Figure 9b**), as Ca^{2+} cations were released in the supernatant solutions (**Figure 8b**). The involvement of both SEA and cationic exchange mechanisms in Co deposition for HAp-R_{37}-Co(1.13)-b is supported by ss NMR spectroscopy (**Figure 2a, Figure S7a**): the observed ^{31}P and ^{1}H chemical shifts are intermediate to those of HAp-R_{37}-Co(0.78) (for which only the cationic exchange mechanism occurs, section 4.1.1.) and HAp-R_{37}-Co(0.80)-b (for which the SEA mechanism occurs almost exclusively) indeed.

Regardless of the deposition mechanisms, Co^{2+} cations are present as highly dispersed surface species on dried samples (**Figure 6**) by interacting with ≡P–O^- groups and by being localized in substitution of the surface Ca crystalline sites (cationic exchange) (**Figure 9b**). Contrary to the Co^{2+} cations immobilized *via* a cationic exchange mechanism, which high dispersion was found to be preserved after annealing at 500 °C, the Co^{2+} cations deposited by a SEA mechanism onto phosphate terminations are not as stable and sinter upon annealing (**Figure 6**), resulting in the formation of Co_3O_4 nanoparticles even for a Co loading as low as 0.8 wt% (HAp-R_{37}-Co(0.80)-b in **Figure 5**).

4.2 Platelet-like HAp

4.2.1 Co immobilization at natural pH

The under-stoichiometric HAp support (bulk Ca/P = 1.57, **Table 1**) with a platelet morphology terminated by a non-crystalline surface layer behaves differently compared to the crystalline surfaces of rods exhibiting higher bulk Ca/P ratios. Its dissolution at acidic pH was found to be promoted (**Figure 8a**) and its surface is highly Ca-deficient (**Figure S4**) with a composition close to that of OCP. This HPO_4^{2-}-enriched highly defective external layer promotes the

lability/exchangeability of ions (**Figure 9c**) between the surface and the solution [53] and, hence, the Co immobilization ability compared to crystallized rods (**Table 2**). According to XPS, this process remains a surface-mediated mechanism (**Figure 6**). The similar chemical down shift of the ^{31}P NMR signals observed for HAp-P_{37}-Co(0.86) and HAp-R_{37}-Co(0.8)-b (**Figure 2b**) indicates, however, a rather close proximity of the Co species with the PO_4^{3-} and/or HPO_4^{2-} groups present inside the external layer. Unlike SEA of Co with the surface terminated ≡P–O^- groups of rod-like HAps, almost no changes were observed after thermal treatment of HAp-P_{37}-Co(0.86). Co^{2+} cations therefore remain as highly dispersed species inside the external non apatitic surface layer of the latter sample and their accessibility to any catalytic reactant (top surface) therefore remains questionable.

4.2.2 Co immobilization in basified medium

While basification of the HAp-P_{37} suspension prior to addition of the Co precursor salt also increased the Co loading in the corresponding samples, a drop in Co surface accessibility was recorded by XPS (**Figure 6**). According to **Figure 8a** (◆), a limited dissolution-precipitation process takes place for HAp-P_{37}-Co(1.20)-b compared to the HAp-P_{37} (◆) and HAp-P_{37}-Co(0.86) (◆). In addition, a high concentration in Co^{2+} cations in a basified medium may allow the incomplete hydrolysis of the OCP-like layer to a HAp-like one to be pursued in the course of the Co immobilization process (**Eq. 6**), finally resulting in the incorporation of the Co^{2+} cations in the HAp-like outer layer (**Figure 9d**).

$$Ca_8(HPO_4)_2(PO_4)_3{\cdot}5H_2O_{(s)} + (2 - x)\ Co(H_2O)_6^{2+}{}_{(aq)} + (4 - x)\ HO^-_{(aq)} \rightarrow$$

$$Ca_8Co_{2-x}(HPO_4)_x(PO_4)_{6-x}(OH)_{2-x}{\cdot}nH_2O_{(s)} + (13 - x - n)\ H_2O_{(l)} \qquad \textbf{(Eq. 6)}$$

Hence, in these conditions, the formation of under-stoichiometric Co-substituted HAp is likely with a (Ca+Co)/P ratio higher than the Ca/P ratio of the support (**Table 2**). Such a distribution of Co in the cationic crystallographic sites of HAp is consistent with the fact that similar

perturbations of the ^{31}P NMR signals are observed for HAp-P_{37}-Co(1.20)-b and the HAp-R_{37}-Co(x) series (**Figures 2a** and **2b**). In the latter series, Co was exchanged with surface cationic Ca^{2+} crystallographic sites of HAp (section 4.1.1). The relatively low Co concentration monitored by XPS is consistent with a deep surface reconstruction process (**Figure 6**, ◆). Such a burying of Co^{2+} cations into the bulk (or deepest subsurface) of the outer layers of HAp makes them unlikely to act as catalytic sites.

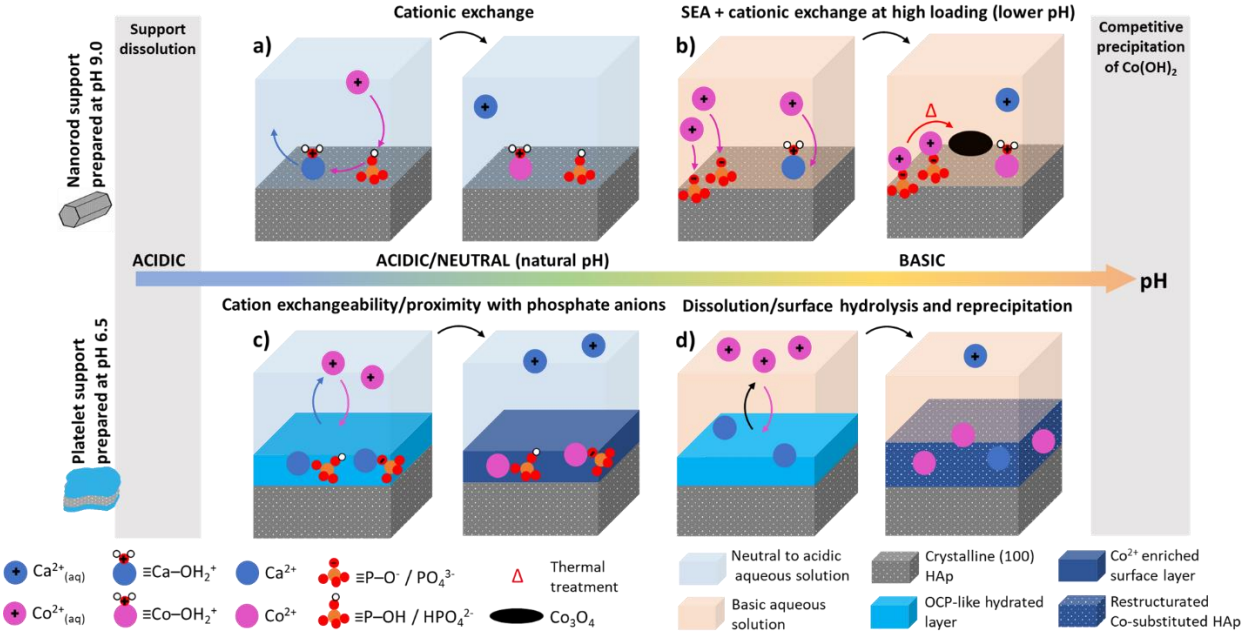

Figure 9: Schematic representation of the main mechanisms involved upon immobilization of Co in an excess of solution depending on the pH of precipitation of the HAp supports (crystalline (100) surface for nanorods or non-apatitic OCP-like hydrated surface for platelets and on the pH applied during the Co deposition (moderately acidic to neutral or basic). On crystalline (100) surfaces involving zig-zag terminations, highly dispersed surface Co species are immobilized by **a)** cationic exchange (possibly through transient protonic exchange of the surface ≡P–OH termination, **Eq. S9-3**, then **Eq. S9-4**) at natural pH and **b)** SEA (**Eq. S9-5**) is favoured in basified medium, whereas for high Co loadings (lower pH), cationic exchange is additionally involved (**Eq. S9-2**). In the presence of the hydrated surface layer of defective HAp prepared at pH 6.5, **c)** dissolution of the support and exchangeability of ions are enhanced at natural pH promoting the dispersion of Co in the hydrated layer that is enriched in PO_4^{3-} and/or HPO_4^{2-} groups and **d)** in basic medium, dissolution still takes place concomitantly with the hydrolysis of the external OCP-like surface layer (**Eq. 6**) in the presence of Co^{2+} cations, resulting in the formation of Co-substituted HAp surface layer. Despite promoting Co trapping, this latter process is detrimental to surface XPS probing of the Co^{2+} cations, however. The high Co dispersion obtained for these four different immobilization mechanisms is preserved upon thermal treatment up to 500 °C, except for SEA on crystalline HAp rods for which the Co species were found to sinter to Co_3O_4 nanoparticles.

5. Conclusion

HAp supports were prepared by controlled precipitation at pH 9.0 and 6.5, leading to (i) a rod-like particle morphology with well crystalline (100) terminations, whose zig-zag organization was modelled by DFT, and (ii) a platelet-like particle morphology embedded in an OCP-like hydrated layer, respectively. Such differences in morphology not only resulted in different Ca/P molar ratios but also in a different ability to release ions in aqueous solution and led to various isoelectric points, *i.e.* 6.6 and 8.0 for rods and platelets, respectively. The impact of these versatile surface properties on the immobilization mechanisms of Co^{2+} cations introduced in an excess of solution was investigated for the first time, considering either natural pH (slightly acidic) or moderately basic media. Overall, increasing the SSA of HAp supports and implementation of a basification of the HAp suspension prior to introduction of the Co precursor salt both allowed to increase the Co loading. The comparison of Co-modified HAps with similar Co loadings clearly shows that four different Co immobilization mechanisms are involved depending on the nature of the HAp support and pH conditions. These mechanisms could be identified by combining bulk and surface characterizations of the as-prepared dried and thermally treated Co-modified HAp materials together with a detailed and systematic examination of the evolution of the pH and the composition of the supernatant solutions:

- At a natural pH on highly crystalline nanorods, while surface dissolution was shown to remain limited, surface cationic exchange occurred as revealed by:

  - the similar final (Ca+Co)/P and Ca/P bulk molar ratio of the Co-modified HAps and the HAp supports, respectively, and

  - the equal quantities of Ca released in solution and Co immobilized on HAp.

  The fact that Co^{2+} cations replaced Ca^{2+} surface crystallographic cationic sites provided strong surface cohesion preventing Co sintering upon thermal treatment at 500 °C. Such

a stability illustrates the high robustness of the atomically dispersed Co species, and makes them of particular interest as potential single atom catalysts.

- In a basified medium, Co species were deposited by SEA on highly crystalline nanorods, through the interactions of Co^{2+} cations with surface terminated ≡P–O^- groups. This is supported by the higher (Ca+Co)/P bulk molar ratio of Co-modified HAps compared to the Ca/P bulk molar ratio of the corresponding HAp support and the lack of Ca^{2+} cations released in the supernatant solutions. Cationic exchange was also found to be additionally involved as the Co loading increased. Despite being initially highly dispersed in the as-prepared dried material, the interaction of Co^{2+} cations with surface ≡P–O^- groups should not be strong enough to avoid sintering upon annealing as Raman spectroscopy revealed the formation of Co_3O_4 nanoparticles after treatment at 500 °C under Ar.
- At natural pH on HAp platelets embedded by an OCP-like hydrated layer, the defectiveness of the under-stoichiometric HAp makes it more sensitive to dissolution and the hydrated surface layer promoted the lability/exchangeability of ions, which facilitated the diffusion of Co ions into this amorphous hydrated layer. Given that the latter is enriched in phosphate species, this leads to close proximity with these anions, as supported by ssNMR. As almost no change was observed on thermal annealing of such sample, the Co deposited species should be stable.
- Finally, implementation of a basification procedure of the HAp suspension prior to the introduction of the Co precursor salt on the defective HAp platelets did not prevent from dissolution and further promoted the surface hydrolysis of the OCP-like surface layer. This accounted for the occurrence of deep restructuration, with the formation of a thermally stable Co-substituted HAp layer. The location of Co^{2+} species at Ca^{2+} cation sites is supported by similar perturbation of ss NMR ^{31}P and ^{1}H signals to those observed

for samples with which cationic exchange was predominantly achieved. In this Co-modified material, the fact that only half of the immobilized cobalt could be probed by XPS obviously questions the intrinsic catalytic reactivity of the buried Co species.

Compared to the commonly used impregnation methods, for which metal speciation is not monitored straightforwardly, the results obtained in the present work show that even for limited Co loadings, Co speciation can be tuned finely by a careful choice of the pH conditions, both for HAp support synthesis and cobalt immobilization. As will be illustrated in a forthcoming paper, the speciation of cobalt is a key parameter for the control of the selectivity in oxidative propane dehydrogenation. In this context, these new insights into the conditions for preparing Co-modified HAp catalysts meet both the requirements for optimizing catalytic performance and the virtuous management of the resources in this critical metal. In addition, the implementation of natural pH conditions, which mimic those used for metal sequestration from wastewaters, led to Co immobilization by cationic exchange on stoichiometric rod-like HAp nanoparticles. This synthesis approach appears as highly promising for preparing robust isolated Co^{2+} cations and even single atom Co catalysts and paves the way for a circular economy on the Co transition metal by combining its recovery from industrial wastes and the creation of robust materials for the catalytic production of value-added compounds.

Acknowledgments

The authors thank Sorbonne University and CNRS for providing funding (Credits récurrents) and access to the analytical equipment used in the present work. C.R. gratefully acknowledges ENS Saclay for financial support (PhD Grant no 3415/2019). The authors also express their gratitude to S. Nowak from Paris Cité for XRF analysis, J.M. Krafft for recording complementary Raman spectra and S. Casale for SEM and TEM characterizations.

References

[1] V.H.J. De Beer, J.C. Duchet, R. Prins, Role of cobalt and nickel in hydrodesulfurization: promoters or catalysts, J. Catal., 72 (1981) 369-372.
[2] D. Laurenti, P. Afanasiev, C. Geantet, Hydrodeoxygenation of guaiacol with CoMo catalysts. Part I: Promoting effect of cobalt on HDO selectivity and activity, Appl. Catal. B-Environ., 101 (2011) 239-245.
[3] R. Munirathinam, D. Pham Minh, A. Nzihou, Effect of the Support and Its Surface Modifications in Cobalt-Based Fischer–Tropsch Synthesis, Ind. Eng. Chem. Res., 57 (2018) 16137-16161.
[4] R. Munirathinam, D. Pham Minh, A. Nzihou, Hydroxyapatite as a new support material for cobalt-based catalysts in Fischer-Tropsch synthesis, Int. J. Hydrogen Energy, (2019).
[5] K. Elkabouss, M. Kacimi, M. Ziyad, S. Ammar, F. Bozon-verduraz, Cobalt-exchanged hydroxyapatite catalysts: magnetic studied, spectroscopic investigations, performance in 2-butanol and ethane oxidative dehydrogenations, J. Catal., 226 (2004) 16-24.
[6] Z. Li, A.W. Peters, A.E. Platero-Prats, J. Liu, C.-W. Kung, H. Noh, M.R. DeStefano, N.M. Schweitzer, K.W. Chapman, J.T. Hupp, Fine-tuning the activity of metal–organic framework-supported cobalt catalysts for the oxidative dehydrogenation of propane, J. Amer. Chem. Soc., 139 (2017) 15251-15258.
[7] M.-X. Huang, X. Wu, X.-D. Yi, G.-B. Han, W.-S. Xia, H.-L. Wan, Highly dispersed CoO_x in layered double oxides for oxidative dehydrogenation of propane: guest–host interactions, RSC Adv., 7 (2017) 14846-14856.
[8] E.C. Tyo, C. Yin, M. Di Vece, Q. Qian, G. Kwon, S. Lee, B. Lee, J.E. DeBartolo, S. Seifert, R.E. Winans , R. Si, B. Ricks, S. Goergen, M. Rutter, B. Zugic, M. Flytzani-Stephanopoulos, Z.W. Wang, R.E. Palmer, M. Neurock, S. Vajda, Oxidative Dehydrogenation of Cyclohexane on Cobalt Oxide (Co_3O_4) Nanoparticles: The Effect of Particle Size on Activity and Selectivity, ACS Catal., 2 (2012) 2409−2423.
[9] S. Lee, A. Halder, G.A. Ferguson, S. Seifert, R.E. Winans, D. Teschner, R. Schlögl, V. Papaefthimiou, J. Greeley, L.A. Curtiss, S. Vajda, Subnanometer cobalt oxide clusters as selective low temperature oxidative dehydrogenation catalysts, Nat. Commun., 10 (2019) 954.
[10] S. Dzwigaj, D. Reja, S. Koné-Guira, A. Miche, G. Costentin, C. Thomas, Cobalt on dealuminated-Siβ as a catalyst for the oxidative dehydrogenation of propane, Appl. Catal. A-Gen., 657 (2023) 119119.
[11] Z. Boukha, J. González-Prior, B. de Rivas, J.R. González-Velasco, R. López-Fonseca, J.I. Gutiérrez-Orti, Synthesis, characterisation and behaviour of Co/hydroxyapatite catalysts in the oxidation of 1,2-dichloroethane, Appl. Catal. B-Environ., 190 (2016) 125-136.
[12] Z. Opre, T. Mallat, A. Baiker, Epoxidation of styrene with cobalt-hydroxyapatite and oxygen in dimethylformamide: A green technology?, J. Catal., 245 (2007) 482-486.
[13] D.C. Carvalho, L.G. Pinheiro, A. Campos, E.R.C. Millet, F.F. de Sousa, J.M. Filho, G.D. Saraiva, E.C. da Silva Filho, M.G. Fonseca, A.C. Oliveira, Characterization and catalytic performances of copper and cobalt-exchanged hydroxyapatite in glycerol conversion for 1-hydroxyacetone production, Appl. Catal. A-Gen., 471 (2014) 39-49.
[14] B.C. Zhou, Q.W. Wang, X.F. Weng, L. He, W.C. Li, A.H. Lu, Regulating Aromatic Alcohols Distributions by cofeeding Methanol with Ethanol over Cobalt-Hydroxyapatite Catalyst, ChemCatChem, 12 (2020) 2341–2347.
[15] Q.N. Wang, X.F. Weng, B.C. Zhou, S.P. Lv, S. Miao, D. Zhang, Y. Han, S.L. Scott, F. Schüth, A.H. Lu, Direct, Selective Production of Aromatic Alcohols from Ethanol Using a Tailored Bifunctional Cobalt−Hydroxyapatite Catalyst, ACS Catal., 9 (2019) 7204−7216.
[16] R. Sun, X. Huang, J. Jiang, W. Xu, S. Zhou, Y. Wei, M. Li, Y. Chen, S. Han, Recent advances in cobalt-based catalysts for efficient electrochemical hydrogen evolution: a review, Dalton Trans., 51 (2022) 15205-15226.
[17] H. Kim, J. Park, I. Park, K. Jin, S.E. Jerng, S.H. Kim, K.T. Nam, K. Kang, Coordination tuning of cobalt phosphates towards efficient water oxidation catalyst, Nat. Commun., 6 (2015) 8253.
[18] X. Lan, W. Zhao, M. Fan, B. Wang, R. Zhang, Local coordination atom and metal types of single-atom catalysts to regulate catalytic performance of C_2H_2 selective hydrogenation, Chem. Eng. Sci., 265 (2023) 118242.

[19] K.J. Schulz, Critical mineral resources of the United States: economic and environmental geology and prospects for future supply, Geological Survey 2017.
[20] D.P. Minh, Design and Applications of Hydroxyapatite-Based Catalysts, John Wiley & Sons 2022.
[21] M. Ben Osman, J.M. Krafft, Y. Millot, F. Averseng, T. Yoshioka, J. Kubo, G. Costentin, Molecular Understanding of the Bulk Composition of Crystalline Nonstoichiometric Hydroxyapatites: Application to the Rationalization of Structure–Reactivity Relationships, Eur. J. Inorg. Chem., 17 (2016) 2709-2720.
[22] G. Costentin, C. Drouet, F. Salles, S. Sarda, Structure and Surface Study of Hydroxyapatite-Based Materials: Experimental and Computational Approaches, in: D.P. Minh (Ed.) Design and Applications of Hydroxyapatite-Based Catalysts, John Wiley & Sons 2022, pp. 73-140.
[23] J.W. Jaworski, S. Cho, Y. Kim, J.H. Jung, H.S. Jeon, B.K. Min, K.-Y. Kwon, Hydroxyapatite supported cobalt catalysts for hydrogen generation, J. Colloid Interf. Sci., 394 (2013) 401-408.
[24] K. Elkabouss, M. Kacimi, M. Ziyad, F. Bozon-Verduraz, Catalytic behaviour of cobalt exchanged hydroxyapatite in the oxidative dehydrogenation of ethane, J. Phys. IV France, 123 (2005) 313-317.
[25] K. El Kabouss, M. Kacimi, M. Ziyad, S. Ammar, A. Ensuque, J.Y. Piquemal, F. Bozon-Verduraz, Cobalt speciation in cobalt oxide-apatite materials: structure–properties relationship in catalytic oxidative dehydrogenation of ethane and butan-2-ol conversion, J. Mater. Chem., 16 (2006) 2453-2463.
[26] T.S. Phan, A.R. Sane, B. Rêgo de Vasconcelos, A. Nzihou, P. Sharrock, D. Grouset, D. Pham Minh, Hydroxyapatite supported bimetallic cobalt and nickel catalysts for syngas production from dry reforming of methane, Appl. Catal. B-Environ., 224 (2018) 310-321.
[27] S. Campisi, M.G. Galloni, F. Bossola, A. Gervasini, Comparative performance of copper and iron functionalized hydroxyapatite catalysts in NH_3-SCR, Catal. Commun., 123 (2019) 79-85.
[28] C. Lv, H. Liang, H. Chen, L. Wu, Hydroxyapatite supported Co_3O_4 catalyst for enhanced degradation of organic contaminants in aqueous solution: Synergistic visible-light photo-catalysis and sulfate radical oxidation process, Microchem. J., 149 (2019) 103959.
[29] D. Misra, R. Bowen, B. Wallace, Adhesive bonding of various materials to hard tooth tissues. VIII. Nickel and copper ions on hydroxyapatite; role of ion exchange and surface nucleation, J. Colloid Interf. Sci., 51 (1975) 36-43.
[30] X. Pan, J. Wang, D. Zhang, Sorption of cobalt to bone char: Kinetics, competitive sorption and mechanism, Desalination, 249 (2009) 609-614.
[31] A. Bhattacharjee, A. Gupta, M. Verma, M.P. Anand, P. Sengupta, M. Saravanan, I. Manna, K. Balani, Antibacterial and magnetic response of site-specific cobalt incorporated hydroxyapatite, Ceram. Int., 46 (2020) 513-522.
[32] A.N. Amenaghawon, C.L. Anyalewechi, H. Darmokoesoemo, H.S. Kusuma, Hydroxyapatite-based adsorbents: Applications in sequestering heavy metals and dyes, J. Env. Manag., 302 (2022) 113989.
[33] S. Kato, S. Kagawa, K. Saito, M. Ogasawara, Incorporation and deposition behaviors of Cu and Ni ions into hydroxyapatite channels by heat treatment, J. Phys. Chem. Solids, 177 (2023) 111287.
[34] J.J. Middelburg, R.N. Comans, Sorption of cadmium on hydroxyapatite, Chem. Geol., 90 (1991) 45-53.
[35] M. Fedoroff, J. Jeanjean, J. Rouchaud, L. Mazerolles, P. Trocellier, P. Maireles-Torres, D. Jones, Sorption kinetics and diffusion of cadmium in calcium hydroxyapatites, Solid State Sci., 1 (1999) 71-83.
[36] D. Marchat, D. Bernache-Assollant, E. Champion, Cadmium fixation by synthetic hydroxyapatite in aqueous solution—Thermal behaviour, J. Hazard. Mater., 139 (2007) 453-460.
[37] Y. Xu, H. Tang, P. Wu, M. Chen, Z. Shang, J. Wu, N. Zhu, Manganese-doped hydroxyapatite as an effective adsorbent for the removal of Pb(II) and Cd(II), Chemosphere, 321 (2023) 138123.
[38] S. Campisi, C. Castellano, A. Gervasini, Tailoring the structural and morphological properties of hydroxyapatite materials to enhance the capture efficiency towards copper(II) and lead(II) ions, New J. Chem., 42 (2018) 4520.
[39] M. Ferri, S. Campisi, M. Scavini, C. Evangelisti, P. Carniti, A. Gervasini, In-depth study of the mechanism of heavy metal trapping on the surface of hydroxyapatite, Appl. Surf. Sci., 475 (2019) 397-409.
[40] M. Akri, S. Shu Zhao, X. Li, K. Zang, A.F. Lee, M.A. Isaacs, W. Xi, Y. Gangarajula, J. Luo, Y. Ren, Y.T. Cui, L. Li, Y. Su, X. Pan, W. Wen, Y. Pan, K. Wilson, L. Li, B. Qiao, H. Ishii, Y.F. Liao, A. Wang, X. Wang, T.

Zhang, Atomically dispersed nickel as coke-resistant active sites for methane dry reforming, Nat. Commun., 10 (2019) 1-10.
[41] A. Corami, S. Mignardi, V. Ferrini, Removal of Lead, Copper, Zinc and Cadmium from Water Using Phosphate Rock, Acta Geol. Sin., 82 (2008) 1223-1228.
[42] L. Wu, W. Forsling, P.W. Schindler, Surface complexation of calcium minerals in aqueous solution: 1. Surface protonation at fluorapatite—water interfaces, J. Colloid Interf. Sci., 147 (1991) 178-185.
[43] D. Gogoi, A.G. Shanmugamani, S.V.S. Rao, T. Kumar, P.K. Sinha, Studies on removal of cobalt from an alkaline waste using synthetic calcium hydroxyapatite, J. Radioanal. Nucl. Chem., 298 (2013) 337-344.
[44] C. Reynaud, C. Thomas, S. Casale, S. Nowak, G. Costentin, Development of a thermodynamic approach to assist the control of the precipitation of hydroxyapatites and associated calcium phosphates in open systems, CrystEngComm, 23 (2021) 4857-4870.
[45] C. Reynaud, C. Thomas, G. Costentin, On the Comprehensive Precipitation of Hydroxyapatites Unraveled by a Combined Kinetic–Thermodynamic Approach, Inorg. Chem., 61 (2022) 3296-3308.
[46] T. Tsuchida, J. Kubo, T. Yoshioka, S. Sakuma, T. Takeguchi, W. Ueda, Influence of preparation factors on Ca/P ratio and surface basicity of hydroxyapatite catalysts, J. Jap. Petrol. Inst., 52 (2009) 51-59.
[47] J.H. Scofield, Hartree-Slater subshell photoionization cross-sections at 1254 and 1487 eV, J. Electron Spectros. Relat. Phenomena, 8 (1976) 129-137.
[48] G. Kresse, J. Furthmüller, Efficient iterative schemes for ab initio total-energy calculations using a plane-wave basis set, Phys. Rev. B, 54 (1996) 11169-11186.
[49] J.P. Perdew, K. Burke, M. Ernzerhof, Generalized gradient approximation made simple, Phys. Rev. Lett., 77 (1996) 3865-3868.
[50] S. Gražulis, D. Chateigner, R.T. Downs, A. Yokochi, M. Quirós, L. Lutterotti, E. Manakova, J. Butkus, P. Moeck, A. Le Bail, Crystallography Open Database–an open-access collection of crystal structures, J.Appl. Cryst, 42 (2009) 726-729.
[51] K. Momma, F. Izumi, VESTA 3 for three-dimensional visualization of crystal, volumetric and morphology data, J. Appl. Crystallogr., 44 (2011) 1272-1276.
[52] M. Ben Osman, S. Diallo-Garcia, V. Herledan, T. Yoshioka, K. Kubo, Y. Millot, G. Costentin, Discrimination of Surface and Bulk Structure of Crystalline Hydroxyapatite Nanoparticles by NMR, J. Phys. Chem. C, 119 (2015) 23008-23020.
[53] J. Gómez-Morales, M. Iafisco, J.M. Delgado-López, S. Sarda, C. Drouet, Progress on the preparation of nanocrystalline apatites and surface characterization: Overview of fundamental and applied aspects, Progress in Crystal Growth and Characterization of Materials, 59 (2013) 1-46.
[54] M. Ben Osman, S. Diallo Garcia, J.M. Krafft, C. Methivier, J. Blanchard, T. Yoshioka, J. Kubo, G. Costentin, Control of calcium accessibility over hydroxyapatite by post precipitation steps: influence on the catalytic reactivity toward alcohols., Phys. Chem. Chem. Phys., 18 (2016) 27837–27847.
[55] T. Tsuchida, J. Kubo, T. Yoshioka, S. Sakuma, T. Takeguchi, W. Ueda, Reaction of ethanol over hydroxyapatite affected by Ca/P ratio of catalyst, J. Catal., 259 (2008) 183-189.
[56] L. Silvester, J.F. Lamonier, R.N. Vannier, C. Lamonier, M. Capron, A.S. Mamede, F. Pourpoint, A. Gervasini, F. Dumeignil, Structural, textural and acid-base properties of carbonates-containing hydroxyapatites, J. Mater. Chem. A, 2 (2014) 11073-11090.
[57] M. Robin, S. Von Euw, G. Renaudin, S. Gomes, J.M. Krafft, N. Nassif, T. Azaïs, G. Costentin, Insights for OCP Identification and Quantification in the Context of Apatite Biomineralization, CrysEngComm, 22 (2020) 2728-2742.
[58] E. Davies, M.J. Duer, S.E. Ashbrook, J.M. Griffin, Applications of NMR Crystallography to Problems in Biomineralization: Refinement of the Crystal Structure and ^{31}P Solid-State NMR Spectral Assignment of Octacalcium Phosphate, J. Am. Chem. Soc., 134 (2012) 12508-12515.
[59] C.A. Ospina, J. Terra, A.J. Ramirez, M. Farinac, D.E. Ellis, A.M. Rossi, Experimental evidence and structural modeling of nonstoichiometric (0 1 0) surfaces coexisting in hydroxyapatite nano-crystals, Colloids Surf. B: Biointerf., 89 (2012) 15-22.

[60] F. Chiatti, M. Corno, Y. Skhno, G. Martra, P. Ugliengo, Revealing hydroxyapatite nanoparticle surface structure by CO adsorption : a combined B3LYP and infra red study, J. Phys. Chem. C, 117 (2013) 25526-25534.
[61] S. Diallo-Garcia, M. Ben Osman, J.M. Krafft, S. Casale, C. Thomas, J. Kubo, G. Costentin, Identification of Surface Basic Sites and Acid-Base Pairs of Hydroxyapatite, J. Phys. Chem. C, 118 (2014) 12744-12757.
[62] S. Diallo-Garcia, M. Ben Osman, J.M. Krafft, S. Boujday, G. Costentin, Discrimination of infra red fingerprints of bulk and surface POH and OH of hydroxypatites, Catal. Today, 226 (2014) 81–88.
[63] M. Ben Osman, J.M. Krafft, C. Thomas, T. Yoshioka, J. Kubo, G. Costentin, Importance of the Nature of the Active Acid / Base Pairs of Hydroxyapatite Involved in the Catalytic Transformation of Ethanol to n-Butanol Revealed by Operando DRIFTS, ChemCatChem 11 (2019) 1765-1778.
[64] L. Bell, H. Mika, The pH dependence of the surface concentrations of calcium and phosphorus on hydroxyapatite in aqueous solutions, J. Soil Sci., 30 (1979) 247-258.
[65] P. Somasundaran, Y. Wang, Surface chemical characteristics and adsorption properties of apatite, Adsorption on and surface chemistry of hydroxyapatite, Springer 1984, pp. 129-149.
[66] P. Somasundaran, Zeta potential of apatite in aqueous solutions and its change during equilibration, J. Colloid Interface Sci., 27 (1968) 659-666.
[67] P. Ducheyne, C. Kim, S. Pollack, The effect of phase differences on the time-dependent variation of the zeta potential of hydroxyapatite, J. Biomed. Mater. Res., 26 (1992) 147-168.
[68] P.W. Brown, R.I. Martin, An Analysis of Hydroxyapatite Surface Layer Formation, J. Phys. Chem. B, 103 (1999) 1671-1675.
[69] L. Wang, G.H. Nancollas, Calcium orthophosphates: crystallization and dissolution, Chem. Rev., 108 (2008) 4628-4669.
[70] K.H. Gayer, A.B. Garrett, The Solubility of Cobalt Hydroxide, $Co(OH)_2$, in Solutions of Hydrochloric Acid and Sodium Hydroxide at 25 °C, J. Am. Chem. Soc., 72 (1950) 3921-3923.
[71] S. Petit, C. Thomas, Y. Millot, J.M. Krafft, C. Laberty-Robert, G. Costentin, Activation of C-H Bond of Propane by Strong Basic Sites Generated by Bulk Proton Conduction on V-Modified Hydroxyapatites for the Formation of Propene, ChemCatChem, 12 (2020) 2506–2521.
[72] X. He, F. Wang, H. Liu, L. Niu, X. Wang, Synthesis and color properties of the TiO_2@$CoAl_2O_4$ blue pigments with low cobalt content applied in ceramic glaze, J. Amer. Ceram. Soc., 101 (2018) 2578-2588.
[73] B. Kraushaar-Czarnetzki, W.G.M. Hoogervorst, R.R. Andrea, G.A. Emeis, W.H.J. Stork, Characterisation of CoII and CoIII in CoAPO Molecular Sieves, J. Chem. Soc. Faraday Trans., 87 (1991) 891-895.
[74] G.B. Ramírez-Rodríguez, J.M. Delgado-López, J. Gómez-Morales, Evolution of calcium phosphate precipitation in hanging drop vapor diffusion by in situ Raman microspectroscopy, CrystEngComm, 15 (2013) 2206-2212.
[75] V. Hadjiev, M. Iliev, I. Vergilov, The raman spectra of Co_3O_4, J. Phys. C: Solid State Phys., 21 (1988) L199.
[76] L. Canesson, Y. Boudeville, A. Tuel, Local Environment of Phosphorus Atoms in $CoAPO_4$-*n* Molecular Sieves: A ^{31}P NMR Study, J. Amer. Chem. Soc., 119 (1997) 10754-10762.
[77] L. Canesson, A. Tuel, The first observation of 'NMR-invisible phosphorus' in cobalt-substituted aluminophosphate molecular sieves, Chem. Comm., 2 (1997) 241-242.
[78] G. Mali, A. Ristić, V. Kaučič, ^{31}P NMR as a Tool for Studying Incorporation of Ni, Co, Fe, and Mn into Aluminophosphate Zeotypes, J. Phys. Chem. B, 109 (2005) 10711-10716.
[79] A. Mondal, M. Kaupp, Quantum-chemical approach to NMR chemical shifts in paramagnetic solids applied to $LiFePO_4$ and $LiCoPO_4$, J. Phys. Chem. Lett., 9 (2018) 1480-1484.
[80] G. Giasson, P.H. Tewari, Hydrolysis of Co (II) at elevated temperatures, Can. J. Chem., 56 (1978) 435-440.

Graphical abstract

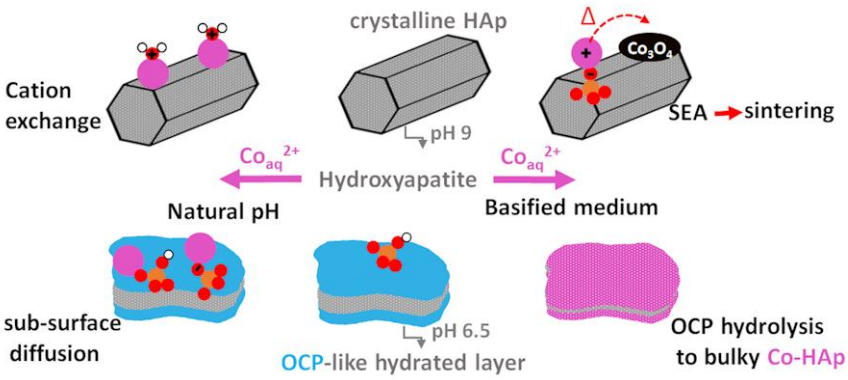

SUPPLEMENTARY INFORMATION

Surface Immobilization Mechanisms of Cobalt ions on Hydroxyapatite catalyst supports.

Corentin Reynaud,[1] Cyril Thomas,[1] Dalil Brouri,[1] Yannick Millot,[1] Antoine Miche[1] and Guylène Costentin[1*]

[1] *Sorbonne Université, CNRS, Laboratoire de Réactivité de Surface (LRS), 4 place Jussieu, 75005 Paris, France*

*Corresponding author: guylene.costentin@sorbonne-universite.fr

SI-1. DFT calculation

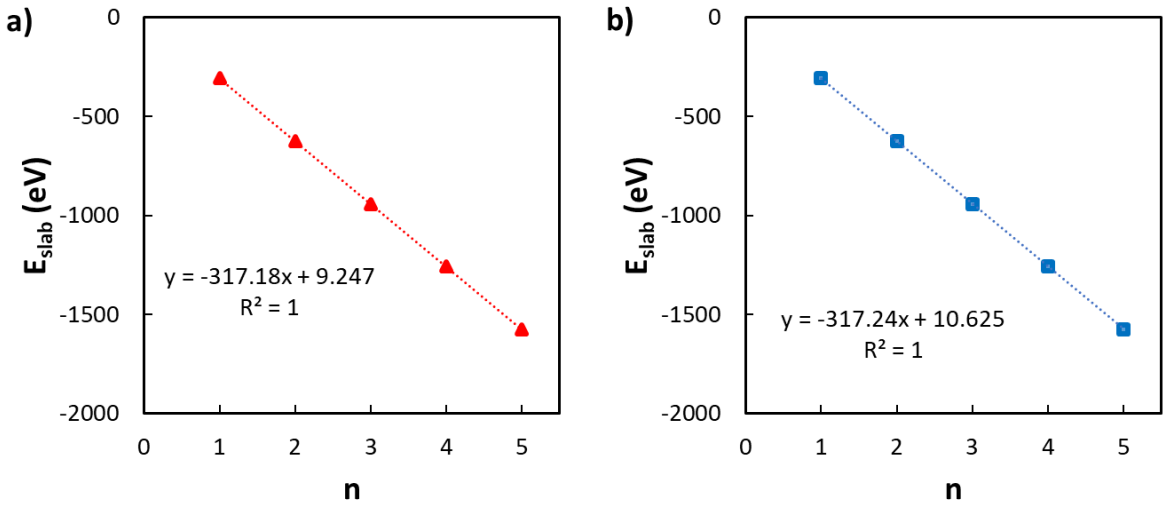

Figure S1: Calculated slab energies versus the number of unit cells (*n* from 1 to 5) considered for **a)** zig-zag and **b)** flat (100) surfaces (separated from each other with distance *d* = 15 Å).

SI-2. XRD

Laboratory X-ray diffraction patterns were recorded with a Brucker D8 Advance diffractometer equipped with a copper source ($\lambda_{Cu\text{-}K\alpha1}$ = 1.54056 Å and $\lambda_{Cu\text{-}K\alpha2}$ = 1.54439 Å) and a LynxEye detector. XRD patterns (**Figure S2**) were recorded by 0.02° steps. From comparison with the ICDD reference card n° 00-009-0432, it is found that the as-synthesized supports exhibit the HAp structure and that Co deposition neither affect the crystallinity of the HAp supports nor leads to the formation of any additional crystalline phase.

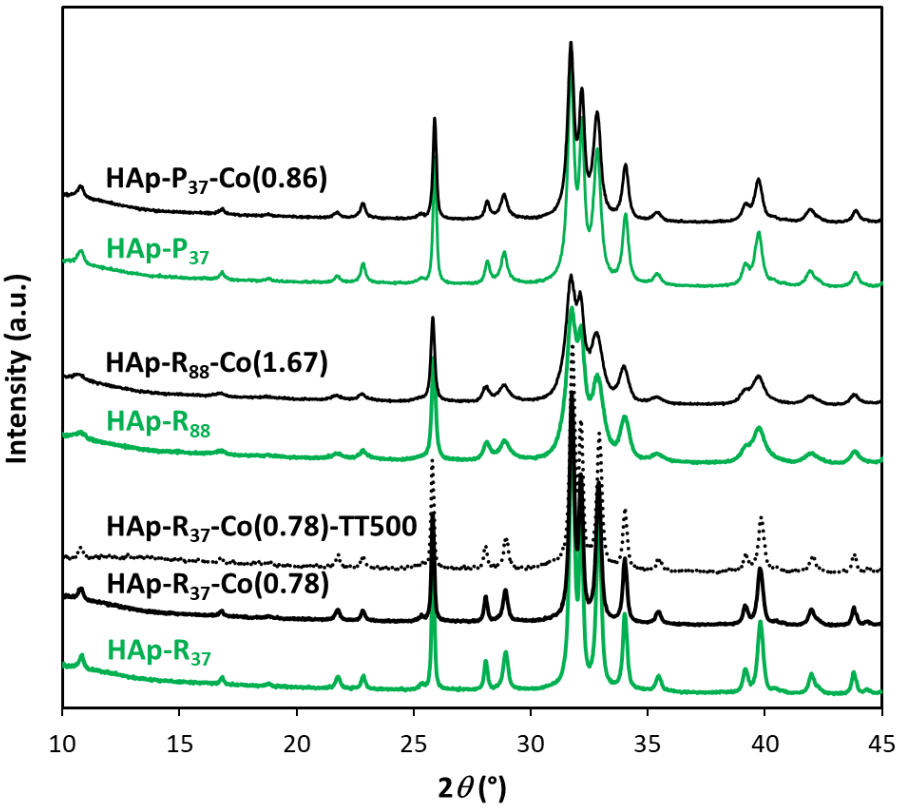

Figure S2: XRD patterns of the HAp supports (green lines) and of representative Co-modified HAp samples prepared at natural pH, samples dried at RT (black solid lines) and sample thermally treated at 500 °C (black dotted line).

SI-3. SEM and TEM characterizations

Morphologic analysis of the dried HAp supports at low magnification was performed using a **SEM-FEG Hitachi SU-70** microscope. The samples were fixed on an alumina SEM support with a carbon adhesive tape and were observed without any metal coating. Secondary electron detector (SE-Lower) was used to observe the samples. The low accelerating voltage was 1 kV to prevent charging effects of the insulating HAps and the working distance was around 10 to 15 mm. As already reported in a previous study [1], **Figure S3a** (left panel) shows that the 2 supports prepared at pH 9.0 exhibit rod-like morphologies with different particle sizes, whereas thin elongated platelets are obtained for the HAp material prepared at pH 6.5. The rod-like morphology of HAp-R_{37} is shown on a TEM micrograph in **Figure S3a** (right panel). After cobalt deposition, no modification could be observed of the rod-like HAp-R_{37} after drying (**Figure S3b** (left panel)) and thermal treatment at 500 °C except for the samples prepared in basified media for which Co_3O_4 nanoparticles could be seen (**Figure S3b** (white arrows on right panel micrograph)).

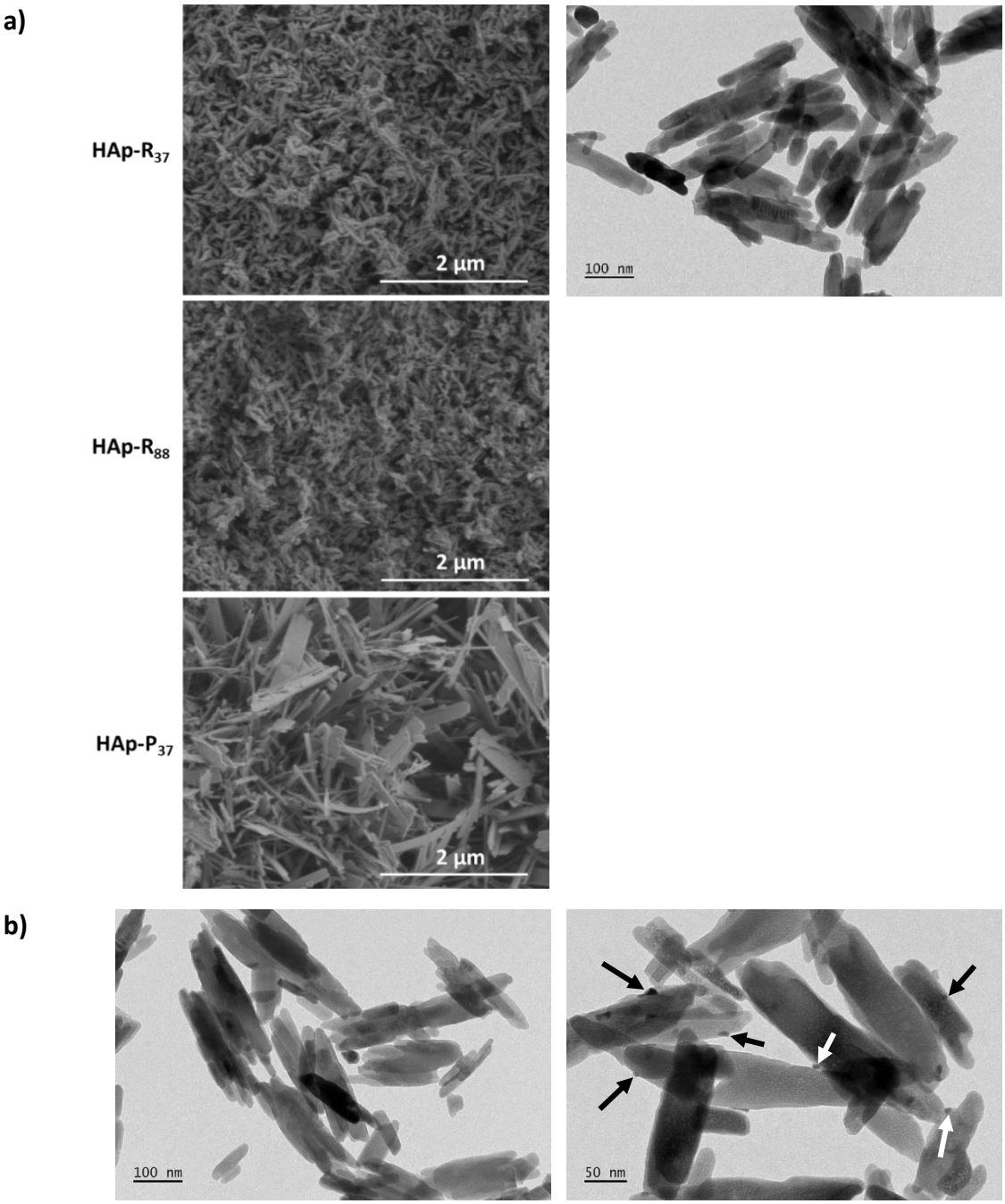

Figure S3: **a)** SEM (left panel) [1] and TEM (right panel)) micrographs of HAp-R_{37}, HAp-R_{88} and HAp-P_{37} supports dried at RT and **b)** TEM micrographs of dried (left panel)) and thermally treated (right panel) HAp-R_{37}-Co(1.13)-b.

SI-4. Surface composition probed by XPS

Comparison of the surface and bulk compositions was performed for several calcium phosphate (CaP) samples: in addition to the three HAp samples considered in the present study (Ca/P bulk ratios ranging from 1.57 to 1.75), additional samples (A-D) have been prepared by adapting the precipitation parameters according to a previous work [2] so as to obtain calcium phosphates with lower Ca/P ratios. Although these metastable calcium phosphates are not straightforward to isolate as pure phases, their composition was validated by XRD, Raman spectroscopy and XRF [2]. The sample labelled A corresponds to dicalcium phosphate anhydrous DCPA octacalcium phosphate (Ca/P = 1); whereas samples B and C mainly contain the OCP phase (Ca/P = 1.33) and sample D corresponds to an amorphous calcium phosphate ACP material (Ca/P = 1.5). As reported in **Figure S4**, the experimental bulk compositions measured by XRF for samples A-D are quite close to the theoretical pure CaP phases. For all calcium phosphates, including HAps, the surface composition probed by XPS systematically show lower Ca/P ratios than those of the bulk. The linear deviation between surface and bulk compositions observed for the whole series of CaP_S (except for HAp-P_{37}) is consistent with the earlier findings reported by Lu *et al.* [3]. Note that, contrary to what has been in a previous study [4], no change with X-Ray irradiation time was observed even after 1 hour under irradiation, which does not support any analysis bias. Moreover, a gradient of surface composition was also reported by ISS [5], and characterization of the surface by CO adsorption-desorption process at low temperature monitored by FTIR showed a lack of calcium accessibility on the top surface compared to terminal HPO_4^{2-} species [5, 6]. Hence, the surface appears to be enriched in HPO_4^{2-} species compared to calcium.

Figure S4 shows that the HAp-P_{37} sample obviously behaves differently compared to the other HAp samples (with significant deviation from the linear regression). This might be ascribed to the presence of an external amorphous layer (**Figure 1d**). Interestingly, the XPS surface

composition of this sample is found to be quite close to that of the OCP-containing sample B (surface Ca/P ratios of 1.10 and 1.13, respectively) (**Figure S4**).

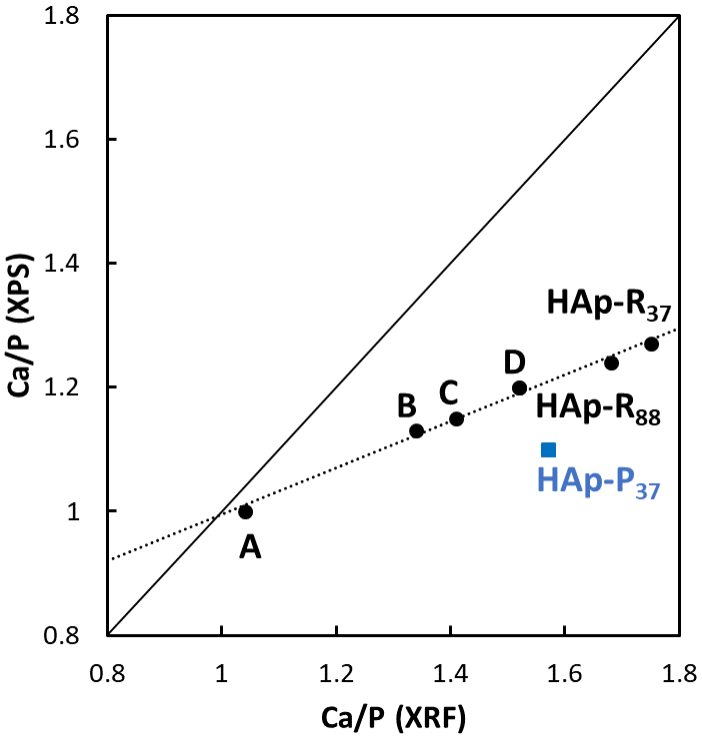

Figure S4: Surface (XPS) *versus* bulk (XRF) Ca/P ratios of HAp-R_{37}, HAp-R_{88}, HAp-P_{37} and of samples A-D (A: DCPA, B and C: mainly OCP and D: mainly ACP) prepared by adapting the precipitation parameters according to a previous work [2]. The solid line represents a surface composition which would be identical to that of the bulk, whereas the dashed line corresponds to the linear regression (R^2 = 0.99) applied to all CaPs, except HAp-P_{37}.

SI-5. surface charge

ζ = f(pH) measurements (**Figure S5)** were achieved using a Litesizer 500 (Anton Paar) apparatus. A suspension of 200 mg of dried sample in 20 mL of ultrapure water containing NH_4NO_3 (10^{-2} mol L^{-1}) was equilibrated for 2 hours, and a fraction was introduced in a 225288-Omega vial. Known amounts of NH_3 (10^{-1} mol L^{-1}) or HNO_3 (10^{-1} mol L^{-1}) were added and equilibrated for 30 min, for the determination of zeta potential at basic and acidic pH, respectively. Collected data have been processed using Kallipe software (Anton Parr). As extracted from the evolution of zeta-potential data with pH **(Figure S5)**, the isoelectric points, 6.6 and 8.0, were found to be significantly different for HAp-R_{37} and for HAp-P_{37}, respectively.

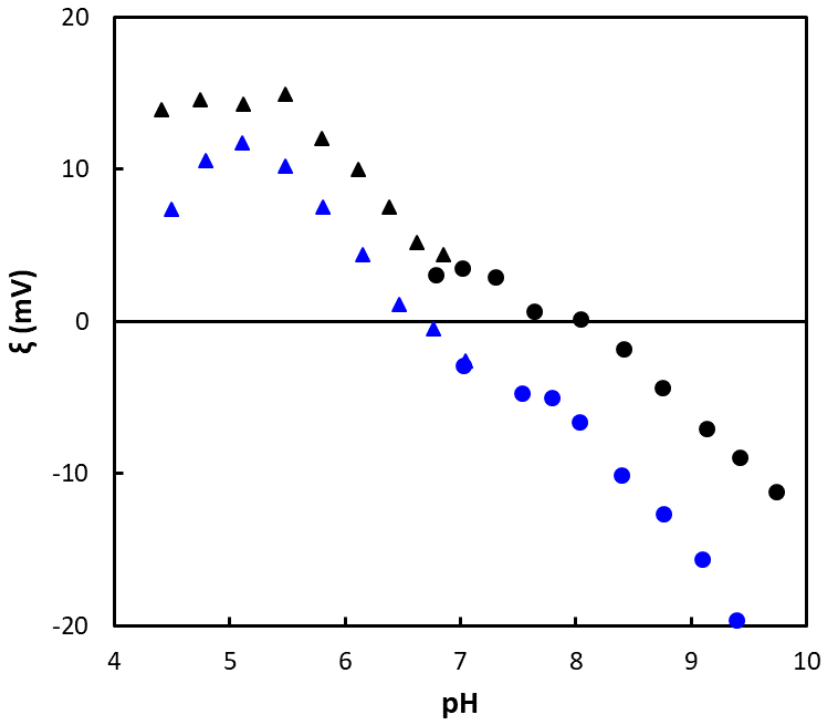

Figure S5: Evolution of the zeta potential with the pH of the suspensions containing HAp-R_{37} (blue) and HAp-P_{37} (black) supports, where triangles and circles corresponds to acidification and basification of the medium, respectively.

Table S5: Comparison of bulk (XRF) and surface (XPS) Ca/P ratios of rod-like (HAp-R_{37}) and platelet-like (HAp-P_{37}) supports, and concentrations of Ca^{2+} cations [Ca] and phosphate species [P] species released in the supernatant solution (ICP-OES) after 2 h equilibration in the presence of the supports and associated [Ca]/[P] ratios.

	Support		**Solution**		
	Ca/P		[Ca]	[P]	[Ca]/[P]
	Bulk	Surface	$\times 10^{-4}$ mol L^{-1}		
HAp-R_{37}	1.75	1.27	1.00	1.15	0.87
HAp-P_{37}	1.57	1.10	2.50	2.05	1.22

SI-6. UV-Vis Diffuse reflectance spectroscopy

UV-Vis DRS spectra were recorded in the range of 200-800 nm with 1 nm steps and a recording speed of 600 nm min^{-1} on a Cary 5000 Varian Spectrometer equipped with a double integration sphere. Background spectrum was recorded with PTFE (polytetrafluoroethylene, Sigma Aldrich) and was subtracted from the sample spectra.

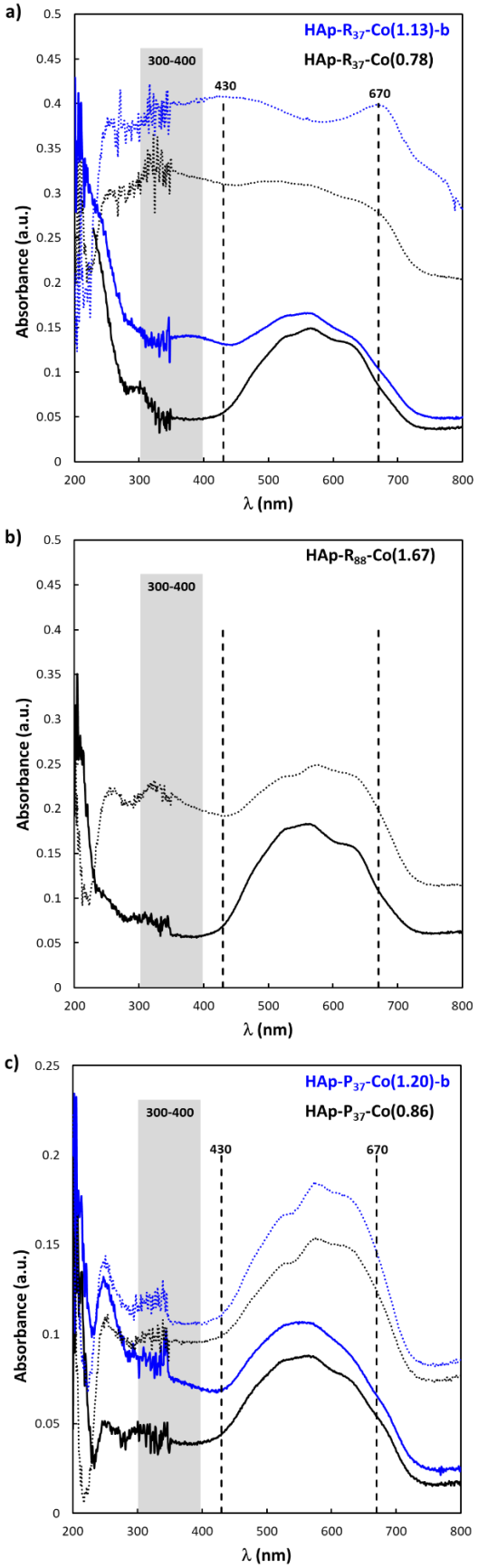

Figure S6: Representative UV-Vis DRS spectra of Co-modified HAp samples **a)** HAp-R_{37} **b)** HAp-R_{88} and **c)** HAp-P_{37} supports, for dried (solid line) or thermally treated at 500 °C (dotted line) samples prepared at natural pH (black spectra) and in basified medium (blue spectra).

SI-7. Influence of cobalt immobilization on HAps on ^{1}H NMR signals

For ^{1}H experiments, an EASY sequence was used to eliminate the probe signal [7]. ^{1}H MAS NMR spectra are performed with a $\pi/2$ pulse duration of 3 µs, a recycle delay of 5 s and a scan number of 8.

Figure S7 shows the modifications of the ^{1}H NMR spectra induced upon deposition of cobalt on HAp-R_{37} and HAp-P_{37} supports. Signals at ~ 0 and 5 ppm of the ^{1}H spectra corresponds to the characteristic fingerprints of protons of hydroxyl groups of HAp and physisorbed water, respectively, [8, 9]. The changes observed on the ^{1}H spectra (chemical shifts and decrease of the intensity of the signals) upon deposition of Co on the two HAp-R_{37} and HAp-P_{37} supports are very similar to those observed in the ^{31}P spectra in **Figures 2a** and **2b**, respectively.

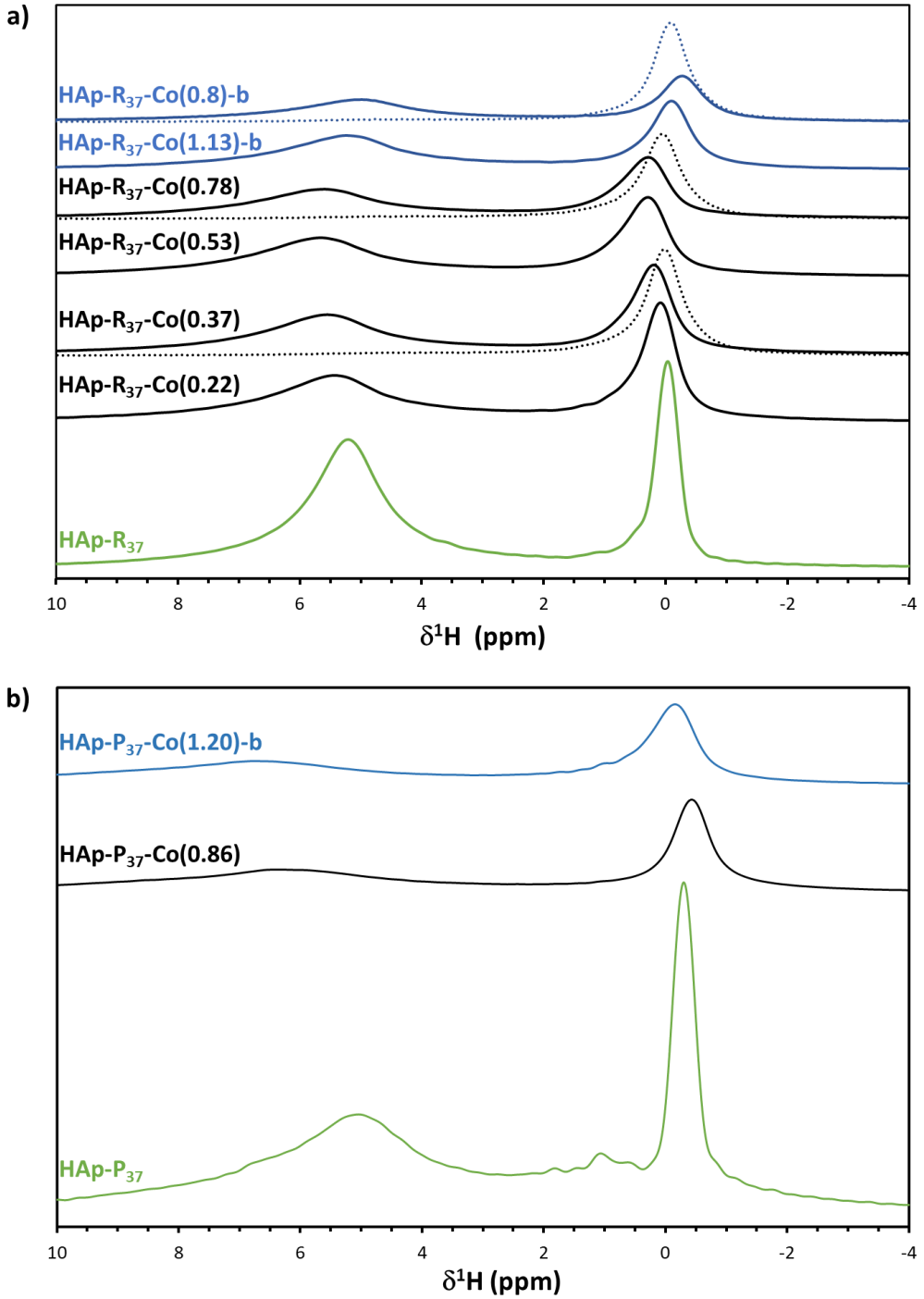

Figure S7: ^{1}H NMR spectra of **a)** HAp-R_{37} and **b)** HAp-P_{37}-based samples. Green spectra arerelated to the supports. Black and blue spectra correspond to samples in which Co was immobilized at natural pH and with a basification procedure prior to the introduction of the Co precursor salt, respectively. Solid and dashed lines are used for dried and 500 °C thermally treated samples, respectively. The intensities of the spectra were normalized by the sample weight introduced into the rotor.

SI-8. Suface *vs* bulk composition

Tables S-8: Comparison of bulk (XRF) and surface (XPS) (Ca+Co)/P ratios measured for dried and thermally treated samples.

Sample	(Ca+Co)/P		
	Bulk (XRF)	Dried (XPS)	Thermally treated (XPS)
HAp-R_{37}-Co(1.13)-b	1.79	1.53	1.46
HAp-R_{37}-Co(0.80)-b	1.82	1.54	1.49
HAp-R_{37}-Co(0.78)	1.75	1.49	1.27
HAp-R_{37}-Co(0.53)	1.75	1.42	1.22
HAp-R_{37}-Co(0.37)	1.77	1.44	1.21
HAp-R_{37}-Co(0.22)	1.77	1.41	1.24
HAp-R_{88}-Co(1.67)	1.68	1.40	1.27
HAp-R_{88}-Co(0.88)	1.69	1.45	-
HAp-R_{88}-Co(0.48)	1.70	1.52	-
HAp-P_{37}-Co(1.20)-b	1.61	1.40	1.06
HAp-P_{37}-Co(0.86)	1.58	1.45	1.05

SI-9. pH profiles

Two typical pH profiles were recorded during the Co deposition processes on HAp-R_{37} (IEP = 6.6) depending on the pH operating conditions (**Figure S9**). After 2 h of equilibration of the HAp-R_{37}-containing suspensions, three phenomena were successively observed for HAp-R_{37}-Co(0.22) and HAp-R_{37}-Co(0.78) prepared at natural pH (**Figure S9a**): (i) an instantaneous acidification (A_1 region), (ii) a slow acidification (A_2 region) followed by (iii) a slow basification (B region) of the media. In the case of the basification of the suspension prior to the introduction of the cobalt precursor salt (**Figure S9b**), the transient slow acidification (A_2 region) was not observed and only two phenomena occurred, (i) an instantaneous acidification (A_1 region) followed by (ii) a rapid basification (B region) of the medium.

These pH profiles are consistent with rapid metal uptake processes, as claimed earlier [10-13]. For the two series of Co deposition on HAp-R_{37}, the first rapid acidification of the media (A_1 region) is associated with the acid-base equilibrium ($K_a = 10^{-9.82}$ at 25 °C) leading to a proton release after introduction of the cobalt precursor salt in the aqueous suspension [14] as described in **Eq. S9-1**.

$$Co(H_2O)_6^{2+}{}_{(aq)} + H_2O_{(l)} \rightleftharpoons Co(H_2O)_5(OH)^{+}{}_{(aq)} + H_3O^{+}{}_{(aq)} \quad \textbf{(Eq. S9-1)}$$

Under the conditions used in the present work, this equilibrium must be only slightly shifted to the production of $Co(H_2O)_5(OH)^{+}{}_{(aq)}$ and protons, which allows us to consider that only $Co(H_2O)_6^{2+}{}_{(aq)}$ species is involved in the surface deposition reactions.

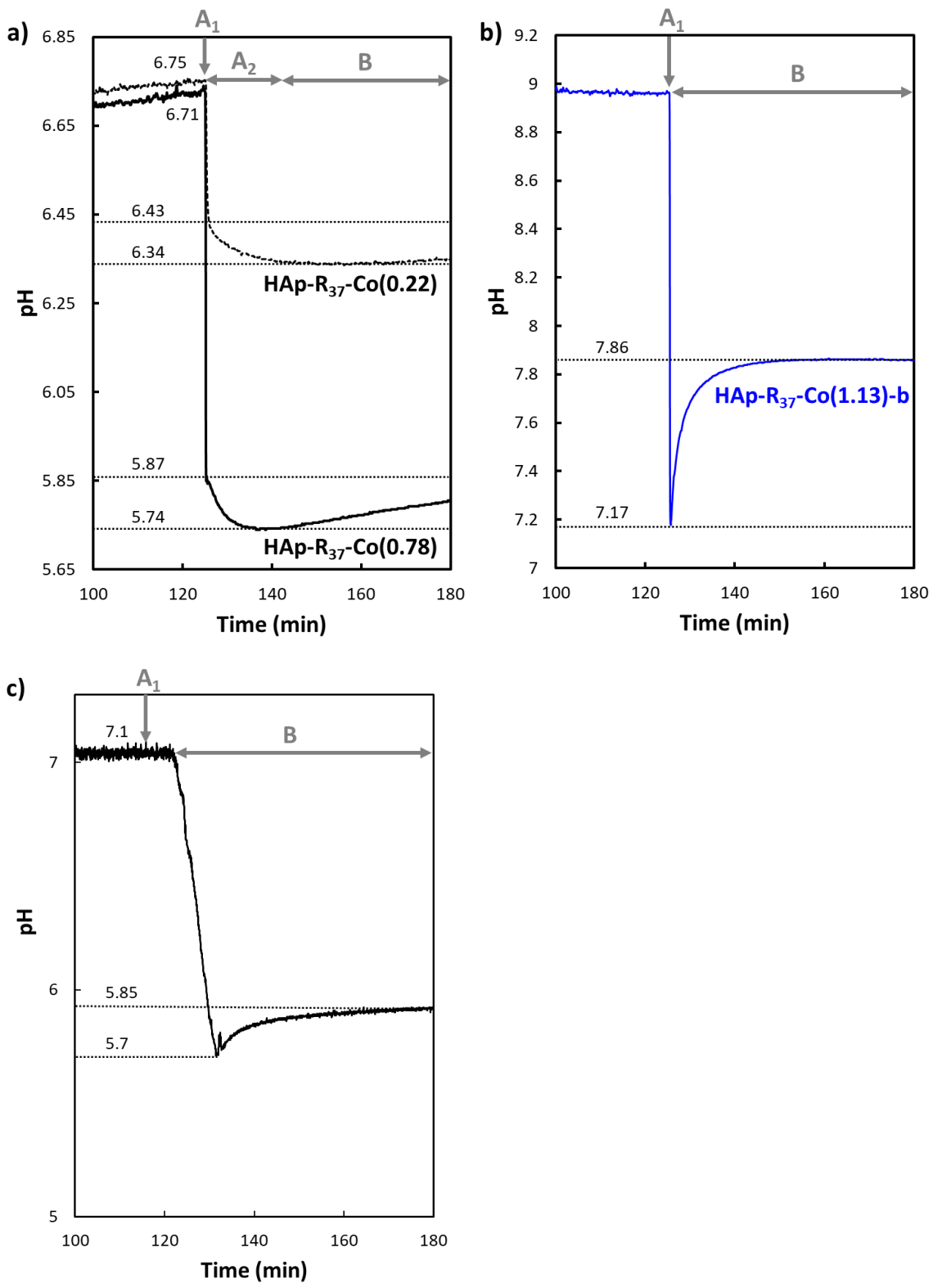

Figure S9: Representative pH profiles recorded during the deposition of cobalt in an excess of solution for the preparation of **a)** HAp-R_{37}-Co(0.22) (dashed line) and HAp-R_{37}-Co(0.78) (solid line) at natural pH, **b)** HAp-R_{37}-Co(1.13)-b with basification of the suspension by NH_3 prior to addition of the cobalt precursor salt in the suspension. A_1, A_2 and B regions correspond to rapid acidification, slow acidification and basification (slow or rapid) of the media, respectively, **c)** blank experiment: introduction of 1 g of HAp (HAp batch prepared under conditions identical to those used for the preparation of HAp-R_{37}) in ultrapure water (initial pH of 5.4), followed by

2 h equilibration time to reach a surface charge comparable with that obtained for HAp-R_{37} (**Figure S9a**) and followed by rapid acidification of the suspension to pH 5.7 by adding diluted HNO_3.

In the pH range of the operating conditions, ≡Ca–OH_2^+ and ≡Co–OH_2^+ terminations predominate over ≡Ca–OH and ≡Co–OH terminations. A direct cationic exchange of Ca^{2+} atoms by Co^{2+} ones, following the reaction described in **Eq. S9-2**, is not expected to be associated with any pH evolution.

$$\equiv Ca–OH_2^{+}{}_{(aq)} + Co(H_2O)_6^{2+}{}_{(aq)} \rightleftharpoons \equiv Co–OH_2^{+} + Ca^{2+}{}_{(aq)} + 6\ H_2O_{(l)} \quad \textbf{(Eq. S9-2)}$$

Such a direct cationic exchange cannot therefore account for the slow acidification observed in the A_2 region of **Figure S9a**. In addition, the decreasing concentration of $Co(H_2O)_6^{2+}{}_{(aq)}$ in solution as the Co deposition progresses should shift the equilibrium described in **Eq. S9-1** to the left and, hence, to a basification of the medium. Given that the blank experiment (similar A1 acidification of the HAp suspension induced by HNO_3, **Figure S9c**) does not show any similar A2 acidification step, it can be deduced that its origin should be definitely associated with a Co immobilization process. It can be proposed that this A_2 acidification region (**Figure S9a**) should rather be attributed to a protonic exchange process of solvated cobalt cations on predominant ≡P–OH surface sites (**Eq. S9-3**).

$$\equiv P–OH + Co(H_2O)_6^{2+}{}_{(aq)} + H_2O_{(l)} \rightleftharpoons \{\equiv P–O^{-}\ ;\ Co(H_2O)_6^{2+}\} + H_3O^{+}{}_{(aq)} \quad \textbf{(Eq. S9-3)}$$

Finally, the basification of the medium (B region in **Figure S9a**) could be ascribed to several processes involving (i) a slow dissolution of the HAp surface that is known to be favoured under acidic conditions [1] and is supported by the increase in pH observed in the blank experiment (**Figure S9c**) and possibly, (ii) a subsequent cationic exchange of Ca^{2+} by Co^{2+} (**Eq. S9-4**).

$$\{\equiv P–O^{-}\ ;\ Co(H_2O)_6^{2+}\} + \equiv Ca–OH_2^{+}{}_{(aq)} + H_3O^{+}{}_{(aq)} \rightleftharpoons \equiv P–OH + \equiv Co–OH_2^{+} + Ca^{2+}{}_{(aq)} + 7\ H_2O_{(l)}$$

(Eq. S9-4)

Such a cationic exchange process is likely to be thermodynamically favoured by both the local increase in $Co(H_2O)_6^{2+}_{(aq)}$ and $H_3O^+_{(aq)}$ concentrations in solution and the low stability of the $\equiv P–O^-$ terminations in this pH range (**Figure 7**).

Hence, these data suggest that the cationic exchange (Ca^{2+} by Co^{2+}, **Eq. S9-2**) observed at natural pH (slightly acidic) conditions may be, at least in part, assisted by a former proton exchange (**Eq. S9-3**).

With a prior basification step (7.9-7.2 > pH > 6.7), Co immobilization no longer leads to slow A_2 acidification (**Figure S9b**). This suggests that Co deposition on the HAp surface takes place according to processes that do not involve acidification. In these conditions, the analysis of the supernatant solutions (**Figure 8**) rather suggests that Co deposition proceeds *via* SEA on the predominant $\equiv P–O^-$ terminations at pH > 6.7 (**Eq. S9-5**),

$$\equiv P–O^- + Co(H_2O)_6^{2+}_{(aq)} \rightleftharpoons \{\equiv P–O^- ; Co(H_2O)_6^{2+}\} \quad \textbf{(Eq. S9-5)}$$

but also, for the highest cobalt concentration, to cation exchange (**Eq. S9-2**).

Finally, the rapid basification of the medium (B region) observed in **Figure S9b** may also result from the shift to the left of the equilibrium described in **Eq. S9-1** as the concentration of $Co(H_2O)_6^{2+}_{(aq)}$ in solution decreases.

References

[1] C. Reynaud, C. Thomas, S. Casale, S. Nowak, G. Costentin, Development of a thermodynamic approach to assist the control of the precipitation of hydroxyapatites and associated calcium phosphates in open systems, CrystEngComm, 23 (2021) 4857-4870.

[2] C. Reynaud, C. Thomas, G. Costentin, On the Comprehensive Precipitation of Hydroxyapatites Unraveled by a Combined Kinetic–Thermodynamic Approach, Inorg. Chem., 61 (2022) 3296-3308.

[3] H.B. Lu, C.T. Campbell, D.J. Graham, B.D. Ratner, Surface Characterization of Hydroxyapatite and Related Calcium Phosphates by XPS and TOF-SIMS, Anal. Chem., 72 (2000) 2886-2894.

[4] C.C. Chusuei, D.W. Goodman, M.J. Van Stipdonk, D.R. Justes, E.A. Schweikert, Calcium Phosphate Phase Identification Using XPS and Time-of-Flight Cluster SIMS, Anal. Chem., 71 (1999) 149-153.

[5] M. Ben Osman, S. Diallo Garcia, J.M. Krafft, C. Methivier, J. Blanchard, T. Yoshioka, J. Kubo, G. Costentin, Control of calcium accessibility over hydroxyapatite by post precipitation steps:

influence on the catalytic reactivity toward alcohols., Phys. Chem. Chem. Phys., 18 (2016) 27837–27847.
[6] S. Diallo-Garcia, M. Ben Osman, J.M. Krafft, S. Casale, C. Thomas, J. Kubo, G. Costentin, Identification of Surface Basic Sites and Acid-Base Pairs of Hydroxyapatite, J. Phys. Chem. C, 118 (2014) 12744-12757.
[7] C. Jaeger, F. Hemmann, EASY: A simple tool for simultaneously removing background, deadtime and acoustic ringing in quantitative NMR spectroscopy—Part I: Basic principle and applications, Solid state nuclear magnetic resonance, 57 (2014) 22-28.
[8] E. Davies, M.J. Duer, S.E. Ashbrook, J.M. Griffin, Applications of NMR Crystallography to Problems in Biomineralization: Refinement of the Crystal Structure and ^{31}P Solid-State NMR Spectral Assignment of Octacalcium Phosphate, J. Am. Chem. Soc., 134 (2012) 12508-12515.
[9] M. Ben Osman, S. Diallo-Garcia, V. Herledan, T. Yoshioka, K. Kubo, Y. Millot, G. Costentin, Discrimination of Surface and Bulk Structure of Crystalline Hydroxyapatite Nanoparticles by NMR, J. Phys. Chem. C 119 (2015) 23008-23020.
[10] J.J. Middelburg, R.N. Comans, Sorption of cadmium on hydroxyapatite, Chem. Geol., 90 (1991) 45-53.
[11] J.W. Jaworski, S. Cho, Y. Kim, J.H. Jung, H.S. Jeon, B.K. Min, K.-Y. Kwon, Hydroxyapatite supported cobalt catalysts for hydrogen generation, J. Colloid Interf. Sci., 394 (2013) 401-408.
[12] M. Fedoroff, J. Jeanjean, J. Rouchaud, L. Mazerolles, P. Trocellier, P. Maireles-Torres, D. Jones, Sorption kinetics and diffusion of cadmium in calcium hydroxyapatites, Solid State Sci., 1 (1999) 71-83.
[13] D. Marchat, D. Bernache-Assollant, E. Champion, Cadmium fixation by synthetic hydroxyapatite in aqueous solution—Thermal behaviour, J. Hazard. Mater., 139 (2007) 453-460.
[14] G. Giasson, P.H. Tewari, Hydrolysis of Co (II) at elevated temperatures, Can. J. Chem., 56 (1978) 435-440.